Electronic Supplementary Material (ESI) for ChemComm.

Supporting Information

Highly Efficient Deep-Blue OLEDs Based on Hybridized Local and Charge-Transfer Emitters Bearing Pyrene as the Structural Unit

Caixia Fu, [†a] Shuai Luo, [†a] Zhenzhen Li, [†b] Xin Ai,[c] Zhenguo Pang,[a] Chuan Li,[a] Kuan Chen,[a] Liang Zhou,*[b] Feng Li,*[c] Yan Huang,[a] Zhiyun Lu*[a]

[a] Key Laboratory of Green Chemistry and Technology (Ministry of Education), College of Chemistry, Sichuan University, Chengdu 610064, PR China. E-mail: luzhiyun@scu.edu.cn.

[b] State Key Laboratory of Rare Earth Resource Utilization, Changchun Institute of Applied Chemistry, Chinese Academy of Sciences, Changchun 130022, PR China. E-mail: zhoul@ciac.ac.cn.

[†] These authors contributed equally to this work.

Table of contents

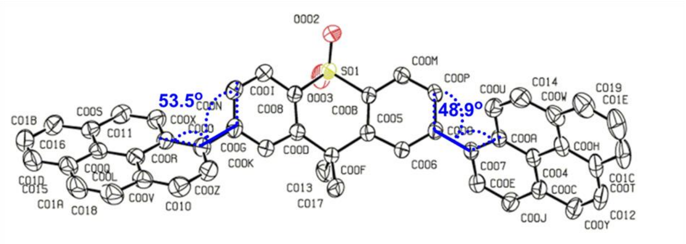

DP-TXO$_2$

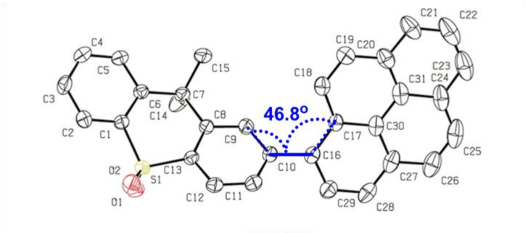

P-TXO$_2$

Figure S1. ORTEP drawings of **DP-TXO$_2$** and **P-TXO$_2$** (ellipsoids at 50% probability, hydrogen atoms removed for clarity).

Table S1. Crystal data and structure refinement for **P-TXO$_2$** and **DP-TXO$_2$**.

Compd.	**P-TXO$_2$**	**DP-TXO$_2$**
Empirical formula	$C_{31}H_{22}O_2S$	$C_{50}H_{33}O_2S$ 0.5C_6H_6
Formula weight	458.54	697.82
Temperature	293.2 K	298.2 K
Crystal system	Triclinic	monoclinic
Space group	*P*-1	*I*2/a
a	8.0078(4) Å	14.6939(3) Å
b	8.2330(4) Å	15.6770(3) Å
c	19.2322(8) Å	31.8617(6) Å
α	95.987(4) deg	90 deg
β	94.228(4) deg	94.2707(16) deg
γ	117.409(5) deg	90 deg
Volume	1108.78(10) Å^3	7319.2(2) Å^3
Z	2	8
Calculated density	1.373 g cm^{-3}	1.267 g cm^{-3}
Absorption coefficient	0.174 mm^{-1}	1.103 mm^{-1}
F(000)	480.0	2920.0
Crystal size	0.35 × 0.25 × 0.05 mm^3	0.5 × 0.4 × 0.3 mm^3
θ-range for datacollection	5.87 to 52.74 deg	8.26 to 145.85 deg
Index ranges	$-10 \leq h \leq 9$	$-14 \leq h \leq 18$
	$-9 \leq k \leq 10$	$-19 \leq k \leq 17$
	$-24 \leq l \leq 16$	$-38 \leq l \leq 39$
Reflections collected	9241	20577
Independent reflections	4515 [*R*(int) = 0.0236]	7179 [*R*(int) = 0.0233]
Data/restraints/parameters	4515/0/309	7179/0/481
Goodness-of-fit on F^2	1.048	1.059
Final *R* indices [$I > 2\sigma(I)$]	$R_1 = 0.0568$, w$R_2 = 0.1351$	$R_1 = 0.0648$, w$R_2 = 0.1826$
R indices (all data)	$R_1 = 0.0830$, w$R_2 = 0.1485$	$\mathrm{R}_1 = 0.0701$, w$R_2 = 0.1909$
Largest diff.peak/hole	0.37 and -0.24 e Å^{-3}	1.20 and -0.37 e Å^{-3}

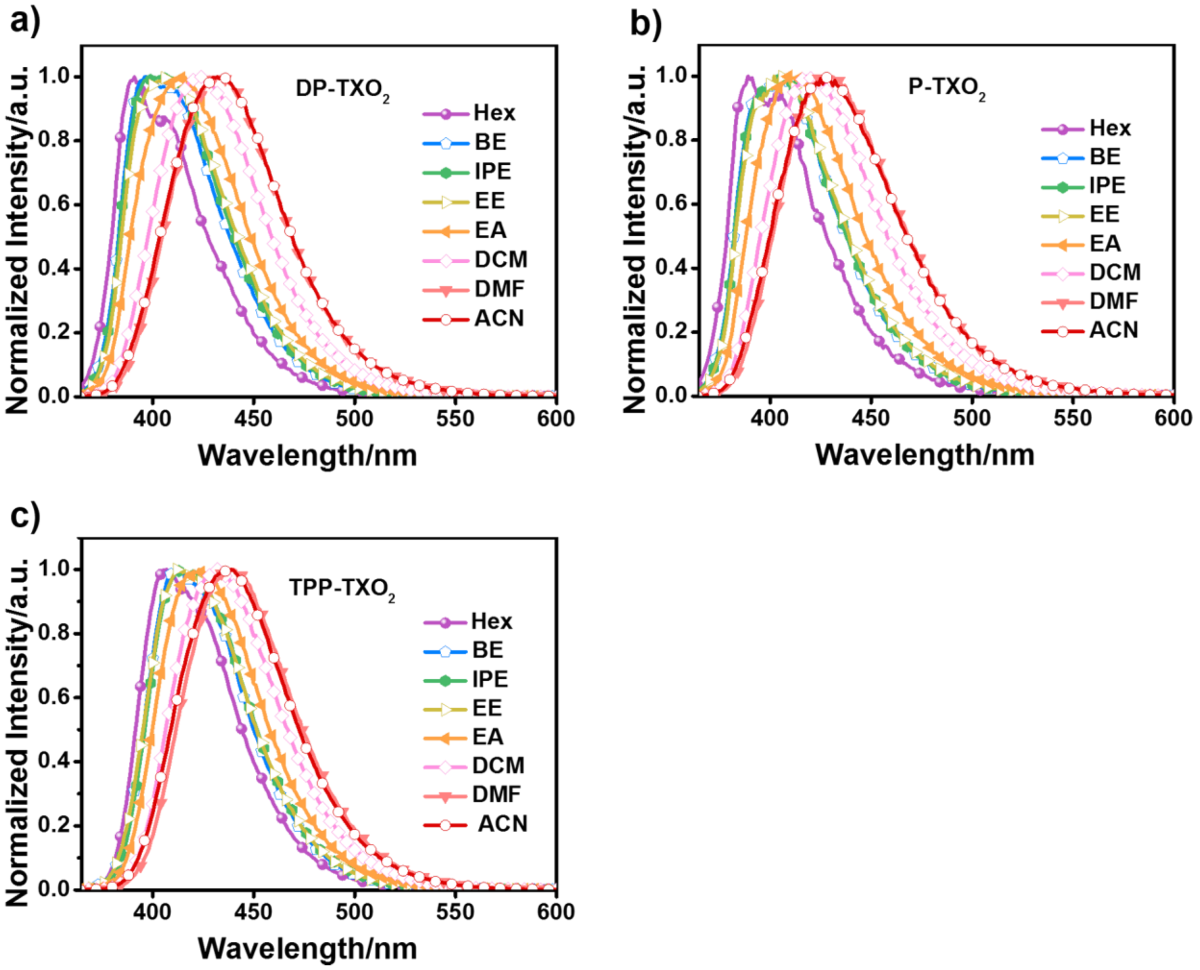

Figure S2. PL emission spectra of a) **DP-TXO$_2$**; b) **P-TXO$_2$**; and c) **TPP-TXO$_2$** in different solvents at λ_{ex} of 350 nm.

The PL emission characteristics of **DP-TXO$_2$**, **P-TXO$_2$** and **TPP-TXO$_2$** in solvents with different polarity, such as *n*-hexane (Hex), butyl ether (BE), isopropyl ether (IPE), ethyl ether (EE), ethyl acetate (EA), dichloromethane (DCM), *N*,*N*-dimethylformamide (DMF) and acetonitrile (ACN), are investigated (Figure S2). In most solvents, the PL spectra of **DP-TXO$_2$** and **P-TXO$_2$** are comparable, but those of **TPP-TXO$_2$** are 5~10 nm red-shifted. This is in consistence with the corresponding absorption characteristics of **DP-TXO$_2$**, **P-TXO$_2$** and **TPP-TXO$_2$** (Figure 2a), indicative of the slightly lower bandgap of **TPP-TXO$_2$** than **DP-TXO$_2$** and **P-TXO$_2$** in both ground and the lowest singlet excited states.

In nonpolar Hex, all the three compounds show PL spectra with fine vibronic structures, implying their LE-featured S_1 states. In solvents with slightly increased polarity like BE and IPE, the PL emission bands of the objective compounds are red-shifted and widened, and platforms rather than peaks are observed in the PL spectra, implying the presence of two different bands in these spectra. In solvents with higher polarity like EA, DCM, DMF and ACN, all these compounds show structureless PL emission bands, reflecting the CT-feature of their S_1 states in polar environments. It is noteworthy that more significant positive solvatochromism are observed in EA, DCM, DMF and ACN than less polar Hex and BE in all these three objective molecules, indicating that in more polar environments, the S_1 states of these compounds should show more significant CT-feature. In addition, among the three objective compounds, **TPP-TXO$_2$** shows the least significant positive solvatochromism effect.

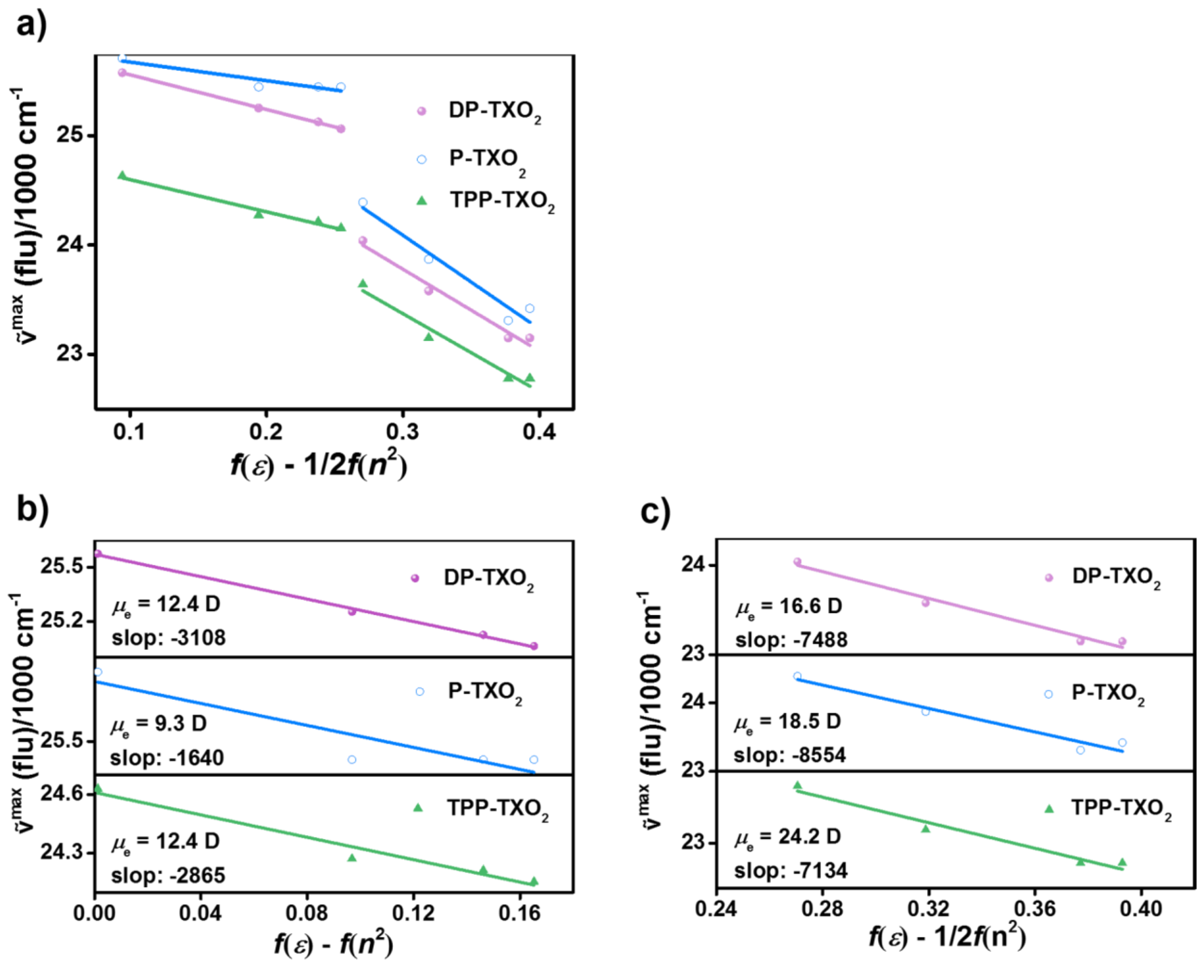

Figure S3. Lippert-Mataga plots of the objective compounds. a) The energies of the fluorescence emission maxima ($\tilde{\nu}^{max}$(flu)) of the compounds against the solvent polarity parameter $f(\varepsilon) - 1/2f(n^2)$; b) the energies of the LE fluorescence emission maxima ($\tilde{\nu}^{max}$(flu, LE)) of the compounds (in less polar solvents) against the solvent polarity parameter $f(\varepsilon) - f(n^2)$; c) the energies of the CT fluorescence emission maxima ($\tilde{\nu}^{max}$(flu, CT)) of the compounds (in more polar solvents) against the solvent polarity parameter $f(\varepsilon) - 1/2f(n^2)$.

To determine the excited-state dipole moment (μ_e) of the objective molecules, the energies of their fluorescence emission maxima ($\tilde{\nu}^{max}$(flu)) are plotted against the polarity parameter $f(\varepsilon, n)$. Note that according to literature report, for the LE emission bands, the solvent polarity parameter $f(\varepsilon, n)$ is $f(\varepsilon) - f(n^2)$, but for the CT emission bands, the solvent polarity parameter $f(\varepsilon, n)$ is $f(\varepsilon) - 1/2f(n^2)$. Here, $f(\varepsilon) = \frac{(\varepsilon-1)}{(2\varepsilon+1)}; f(n^2) = \frac{(n^2-1)}{(2n^2+1)}$.[1]

Initially, the energies of $\tilde{\nu}^{max}$(flu) of the fluorescence bands of all the three compounds are plotted against the solvent polarity parameter $f(\varepsilon) - 1/2f(n^2)$. As shown in Figure S3a, for all the three compounds, two straight lines with different slopes are necessary to fit the data, suggesting that the PL spectra of these compounds should consist of two bands with different characters. As the the two lines intersect near the solvent polarity of BE, the higher energies of the fluorescence bands of these compounds are plotted against $f(\varepsilon) - f(n^2)$ in less polar solvents of Hex, BE, IPE and EE; while the lower energies of the fluorescence bands of these compounds are plotted against $f(\varepsilon) - 1/2f(n^2)$ in more polar EA, DCM, DMF and ACN. As depicted in Figure S3b and S3c, in both cases, single straight lines can be used to fit the data, verifying the LE-dominated feature of the S_1 states of the objective compounds in low polarity solvents, and the CT-dominated feature of the S_1 states of the objective compounds in high polarity solvents, respectively.

The excited-state dipole moment (μ_e) of the molecules could be calculated by the corresponding slopes based on the following equation (1):

$$\tilde{\nu}^{max}(flu) = -\frac{1}{2hc\rho^3}\mu_e\left(\mu_e - \mu_g\right)f(\varepsilon,n) + const \qquad (1)$$

(where ε is the dielectric constant, n is the refractive index, ρ is the Onsager radius of the solute, and μ_g is the ground-state dipole moment of the solute). Here, the ρ values of **DP-TXO$_2$**, **P-TXO$_2$** and **TPP-TXO$_2$** are calculated to be 6.0, 6.3 and 8.3Å,[2] and the μ_g values of of **DP-TXO$_2$**, **P-TXO$_2$** and **TPP-TXO$_2$** are calculated to be 6.9, 6.9, and 7.2 D, respectively, according to DFT calculation results. Therefore, the dipole moment of the LE state of **DP-TXO$_2$**, **P-TXO$_2$** and **TPP-TXO$_2$** is calculated to be 12.4, 9.3 and 12.4 D, respectively (depicted in Figure S3b); while that of the CT singlet excited state is 16.6, 18.5 and 24.2 D in sequence (depicted in Figure S3c).

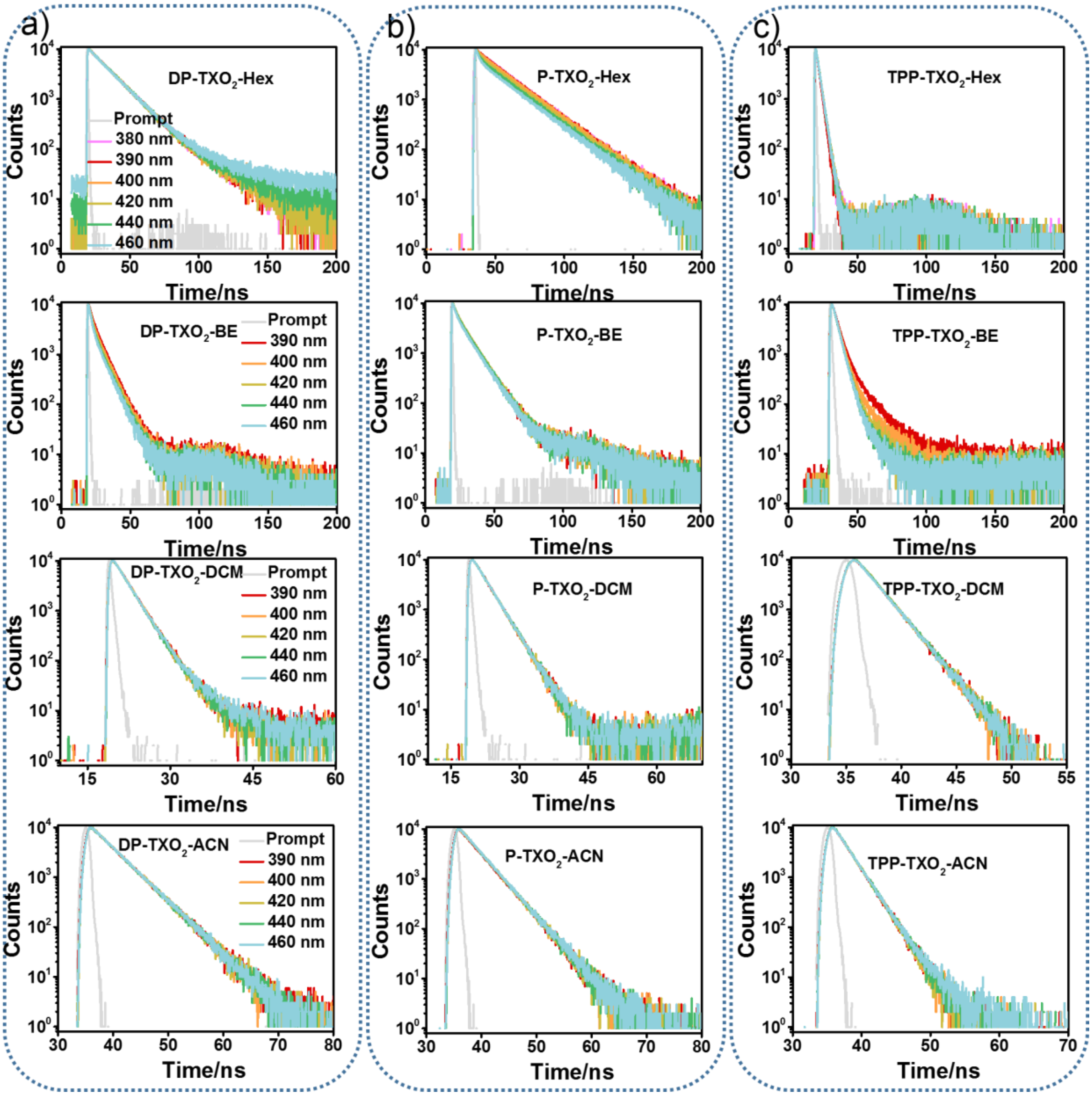

Figure S4. Transient PL decay spectra of: a) **DP-TXO$_2$**; b) **P-TXO$_2$**; and c) **TPP-TXO$_2$** in different solvents at different λ_{em} (at 295 K).

Table S2. Summary of fluorescence lifetimes of the objective compounds in Hex, BE and DCM at different λ_{em} (at 295 K).

		DP-TXO$_2$		**P-TXO$_2$**		**TPP-TXO$_2$**	
Solvent	λ_{em}	lifetime (weight)	χ^2	lifetime (weight)	χ^2	lifetime (weight)	χ^2
Hex	380 nm	τ_1 = 15.7 ns (100%)	1.2	τ_1 = 20.7 ns (100%)	1.2	τ_1 = 2.1 ns (99%) τ_2 = 7.4 ns (1%)	1.1
	390 nm	τ_1 = 15.7 ns (100%)	1.3	τ_1 = 3.8 ns (7%) τ_2 = 20.8 ns (93%)	1.1	τ_1 = 2.2 ns (99%) τ_2 = 7.8 ns (1%)	1.1
	400 nm	τ_1 = 15.7 ns (100%)	1.3	τ_1 = 2.4 ns (13%) τ_2 = 20.7 ns (87%)	1.1	τ_1 = 2.3 ns (100%)	1.3
	420 nm	τ_1 = 15.7 ns (100%)	1.3	τ_1 = 2.2 ns (27%) τ_2 = 20.7 ns (73%)	1.0	τ_1 = 2.3 ns (100%)	1.1
	440 nm	τ_1 = 15.6 ns (100%)	1.2	τ_1 = 2.1 ns (39%) τ_2 = 20.6 ns (61%)	1.0	τ_1 = 2.3 ns (100%)	1.3
	460 nm	τ_1 = 15.6 ns (100%)	1.2	τ_1 = 2.1 ns (50%) τ_2 = 20.7 ns (50%)	1.0	τ_1 = 2.3 ns (100%)	1.1
BE	390 nm	τ_1 = 2.0 ns (49%) τ_2 = 7.2 ns (51%)	1.2	τ_1 = 2.4 ns (39%) τ_2 = 10.2 ns (61%)	1.2	τ_1 = 2.0 ns (94%) τ_2 = 7.3 ns (6%)	1.1
	400 nm	τ_1 = 1.8 ns (58%) τ_2 = 7.2 ns (42%)	1.2	τ_1 = 2.3 ns (37%) τ_2 = 10.1 ns (63%)	1.2	τ_1 = 1.9 ns (97%) τ_2 = 7.3 ns (3%)	1.2
	420 nm	τ_1 = 1.8 ns (64%) τ_2 = 7.2 ns (36%)	1.3	τ_1 = 2.2 ns (36%) τ_2 = 10.2 ns (64%)	1.2	τ_1 = 1.9 ns (97%) τ_2 = 7.0 ns (3%)	1.0
	440 nm	τ_1 = 1.8 ns (69%) τ_2 = 7.2 ns (31%)	1.3	τ_1 = 2.1 ns (40%) τ_2 = 10.1 ns (60%)	1.2	τ_1 = 1.8 ns (98%) τ_2 = 6.6 ns (2%)	1.2
	460 nm	τ_1 = 1.8 ns (72%) τ_2 = 7.2 ns (28%)	1.2	τ_1 = 2.1 ns (46%) τ_2 = 10.2 ns (54%)	1.2	τ_1 = 1.8 ns (98%) τ_2 = 6.6 ns (2%)	1.1
DCM	390 nm	τ_1 = 2.4 ns (100%)	1.1	τ_1 = 2.9 ns (100%)	1.2	τ_1 = 1.6 ns (100%)	1.2
	400 nm	τ_1 = 2.4 ns (100%)	1.2	τ_1 = 2.9 ns (100%)	1.1	τ_1 = 1.6 ns (100%)	1.1
	420 nm	τ_1 = 2.4 ns (100%)	1.0	τ_1 = 2.9 ns (100%)	1.1	τ_1 = 1.6 ns (100%)	1.2
	440 nm	τ_1 = 2.2 ns (100%)	1.2	τ_1 = 2.9 ns (100%)	1.1	τ_1 = 1.6 ns (100%)	1.1
	460 nm	τ_1 = 2.2 ns (100%)	1.3	τ_1 = 2.9 ns (100%)	1.1	τ_1 = 1.6 ns (100%)	1.1
ACN	390 nm	τ_1 = 4.1 ns (100%)	1.1	τ_1 = 3.4 ns (100%)	1.0	τ_1 = 2.1 ns (100%)	1.1
	400 nm	τ_1 = 4.1 ns (100%)	1.1	τ_1 = 3.4 ns (100%)	1.1	τ_1 = 2.1 ns (100%)	1.0
	420 nm	τ_1 = 4.1 ns (100%)	1.1	τ_1 = 3.4 ns (100%)	1.1	τ_1 = 2.1 ns (100%)	1.0
	440 nm	τ_1 = 4.1 ns (100%)	1.0	τ_1 = 3.4 ns (100%)	1.0	τ_1 = 2.1 ns (100%)	1.0
	460 nm	τ_1 = 4.1 ns (100%)	1.0	τ_1 = 3.4 ns (100%)	1.1	τ_1 = 2.1 ns (100%)	1.1

For **DP-TXO$_2$**, at varied monitored λ_{em} (380-460 nm), its degassed Hex solution (2×10^{-6} M) shows quite similar mono- exponential PL decay characters, and the lifetime is about 15.7 ns (Figure S4a, Table S2). In more polar DCM and ACN. **DP-TXO$_2$** also shows quite similar mono-exponential PL decay at varied monitored λ_{em} and the lifetime is short. Because by using quinoline sulfate as the reference (φ_{PL} = 0.55, λ_{ex} = 350 nm), the φ_{PL} values of **DP-TXO$_2$** in degassed Hex, DCM and ACN solutions (2×10^{-6} M) are determined to be 0.63, 0.57 and 0.71, respectively, the radiative decay rate constants (k_r) of varying solvents of **DP-TXO$_2$** are calculated to be 4.0×10^7, 2.4×10^8 s^{-1} and 1.7×10^8 s^{-1}, respectively. Since in non-polar Hex, the PL spectra of **DP-TXO$_2$** shows well-resolved vibronic bands, and the PL decay characters of **DP-TXO$_2$** in Hex is mono-exponential, the S_1 state of **DP-TXO$_2$** in Hex should be of relatively pure ^{1}LE feature. While in DCM and ACN, the PL spectrums of **DP-TXO$_2$** are structureless, and the PL decay characters of **DP-TXO$_2$** in DCM and ACN are both mono-exponential. The radiative decay rate constants (k_rs) of **DP-TXO$_2$** in DCM and ACN are similar ($k_{r(DCM)} = 2.4 \times 10^8$ s^{-1}; $k_{r(ACN)} = 1.7 \times 10^8$ s^{-1}), indicative of the ^{1}CT transition nature of **DP-TXO$_2$** in DCM and ACN. It is noteworthy that the $k_{r(LE)}$ of **DP-TXO$_2$** is much smaller than that of the ($k_{r(LE)} \sim 4.0 \times 10^7$ s^{-1}; $k_{r(CT)} \sim 2.0 \times 10^8$ s^{-1}), which should be attributed to the relatively forbidden $S_1 \rightarrow S_0$ transition nature of the pyrene unit in **DP-TXO$_2$**. In BE that is more polar than Hex but less polar than DCM, **DP-TXO$_2$** is observed to show a bi-exponential decay character (τ_1 ~ 2.0 ns; τ_2 ~ 7.2 ns) at every monitored λ_{em} (390-460 nm). More importantly, with increasing monitored λ_{em} from 390 to 460 nm, the contribution of the shorter lifetime component (τ_1 ~ 2.0 ns) increases gradually from 49% to 72%, while that from the longer one (τ_2 ~ 7.2 ns) decreases commensurately from 51% to 28%, as depicted in Table S2. As the ^{1}CT of **DP-TXO$_2$** is demonstrated to show more pronouced positive solvatochromism than the ^{1}LE one, the species with longer τ of ~ 7.2 ns can be safely assigned to the ^{1}LE state of **DP-TXO$_2$**; while the species with shorter τ of ~ 2.0 ns can be safely assigned to the ^{1}CT state of **DP-TXO$_2$**. Therefore, the bi-exponential decay character of **DP-TXO$_2$** in BE reveals clearly the state-mixing of ^{1}LE and ^{1}CT states, hence the HLCT-feature of **DP-TXO$_2$**. Note that although up to date, many HLCT materials have been developed successfully, all of them are reported to show mono- rather than bi-exponential decay characteristics in varying solvents. Hence our findings provide the first direct experimental evidences for the state-mixing of ^{1}LE and ^{1}CT in HLCT compounds.

In the case of **P-TXO$_2$**, at relatively high-energy λ_{em} of 380 nm, its Hex solution (2 × 10^{-6} M) shows a mono-exponential PL decay character with τ of 20.7 ns. But at longer monitored emission wavelengths of 390-460 nm, bi-exponential PL decay (τ_1 ~ 2.2 ns; τ_2 ~ 20.7 ns) are observed. Similar to the solution sample of **DP-TXO$_2$** in BE, with increasing monitored emission wavelengths from 390 to 460 nm, the contribution from the shorter lifetime component (τ_1 ~ 2.2 ns) increases gradually from 7% to 50%, while that from the longer one (τ_2 ~ 20.7 ns) decreases commensurately from 93% to 50%, as depicted in Table S2. These findings suggest that the ^{1}LE and ^{1}CT states of **P-TXO$_2$** should mix even in nonpolar Hex. In BE with slightly higher polarity than Hex, the contribution from ^{1}CT state of **P-TXO$_2$** to the PL emission is found to be more significant, and the average lifetime values are much more shortened than those of the corresponding Hex solution sample in every monitored λ_{em}. In more polar DCM and ACN, **P-TXO$_2$** show not only a structureless PL band, but also a mono-exponential PL decay character at every monitored λ_{em} with a relatively short lifetime of ~ 2.9 ns and ~ 3.4 ns. As the φ_{PL}s of **P-TXO$_2$** in degassed DCM and ACN, are determined to be 0.68 and 0.68, the k_rs of **P-TXO$_2$** in degassed DCM and ACN are estimated to be 2.3 × 10^8 s^{-1} and 2.0 × 10^8 s^{-1}, the $k_{r(CT)}$ of **P-TXO$_2$** is estimated to be about 2.3 × 10^8 s^{-1}, which is identical to that of **DP-TXO$_2$**.

As far as **TPP-TXO$_2$** is concerned, in both Hex and BE, it displays a bi-exponential PL decay feature (τ_1 ~ 2.0 ns; τ_2 ~ 7.0 ns), which should be assigned to its ^{1}CT and ^{1}LE excited states, respectively. In comparison with those of **DP-TXO$_2$** and **P-TXO$_2$**, the lifetime of the ^{1}CT state of **TPP-TXO$_2$** is analogous, but that of the ^{1}LE state is much shortened. This should be attributed to the more extended π-conjugation system of pyrene in **TPP-TXO$_2$** due to the phenyl substitution on its 6-position.[3] In DCM and ACN, the PL decay curve of **TPP-TXO$_2$** could be mono-exponentially fitted ($\tau_{(DCM)}$ ~ 1.6 ns; $\tau_{(ACN)}$ ~ 2.1 ns). As the φ_{PL}s of **TPP-TXO$_2$** in degassed DCM and ACN are determined to be 0.51 and 0.79, the k_rs of **TPP-TXO$_2$**

in degassed DCM and ACN are estimated to be 3.2 $\times 10^8$ s^{-1} and 3.8 $\times 10^8$ s^{-1}, the $k_{r(CT)}$ of **TPP-TXO₂** is estimated to be about 3.5 $\times 10^8$ s^{-1}, which is analogous to the $k_{r(CT)}$ values of **DP-TXO₂** and **P-TXO₂**.

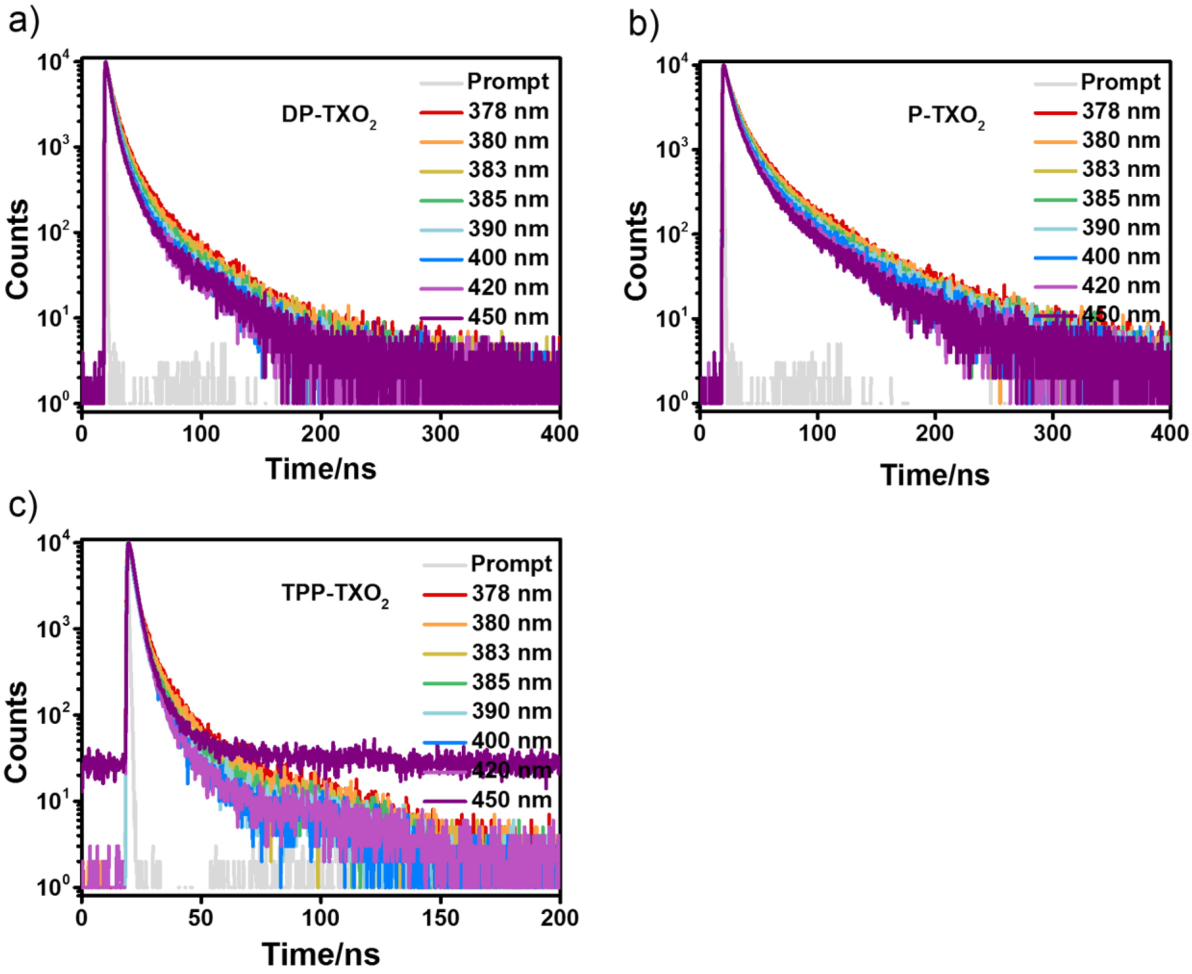

Figure S5. Transient PL decay curves of the 1 wt.%-doped films of: a) **DP-TXO₂**; b) **P-TXO₂**; and c) **TPP-TXO₂** in PMMA matrix at different λ_{em} at 295 K (λ_{ex} = 320 nm).

Table S3. PL lifetimes of the objective compounds in 1 wt.%-doped PMMA films at different λ_{em} at 295 K (λ_{ex} = 320 nm).

	DP-TXO$_2$		**P-TXO$_2$**		**TPP-TXO$_2$**	
λ_{em}	lifetime (weight)	χ^2	lifetime (weight)	χ^2	lifetime (weight)	χ^2
378 nm	τ_1 = 4.1 ns (68%) τ_2 = 12.1 ns (29%) τ_3 = 40.6 ns (3%)	1.0	τ_1 = 5.6 ns (63%) τ_2 = 18.0 ns (33%) τ_3 = 59.2 ns (4%)	1.0	τ_1 = 1.7 ns (75%) τ_2 = 5.5 ns (23%) τ_3 = 23.2 ns (2%)	1.2
380 nm	τ_1 = 3.9 ns (68%) τ_2 = 11.3 ns (29%) τ_3 = 38.2 ns (3%)	1.0	τ_1 = 5.7 ns (65%) τ_2 = 17.8 ns (32%) τ_3 = 58.4 ns (3%)	1.1	τ_1 = 1.9 ns (81%) τ_2 = 6.2 ns (18%) τ_3 = 24.1 ns (1%)	1.1
383 nm	τ_1 = 3.7 ns (68%) τ_2 = 10.5 ns (29%) τ_3 = 35.9 ns (3%)	1.1	τ_1 = 5.5 ns (65%) τ_2 = 16.8 ns (32%) τ_3 = 56.0 ns (3%)	1.1	τ_1 = 1.8 ns (80%) τ_2 = 5.5 ns (19%) τ_3 = 22.5 ns (1%)	1.0
385 nm	τ_1 = 3.8 ns (70%) τ_2 = 10.4 ns (28%) τ_3 = 34.9 ns (2%)	1.0	τ_1 = 5.6 ns (69%) τ_2 = 17.6 ns (28%) τ_3 = 57.7 ns (3%)	1.0	τ_1 = 1.8 ns (79%) τ_2 = 5.2 ns (20%) τ_3 = 20.8 ns (1%)	1.1
390 nm	τ_1 = 3.8 ns (75%) τ_2 = 10.8 ns (23%) τ_3 = 36.3 ns (2%)	1.0	τ_1 = 5.5 ns (71%) τ_2 = 17.5 ns (26%) τ_3 = 58.1 ns (3%)	1.1	τ_1 = 1.9 ns (83%) τ_2 = 5.4 ns (15%) τ_3 = 20.1 ns (2%)	1.1
400 nm	τ_1 = 3.8 ns (76%) τ_2 = 10.4 ns (22%) τ_3 = 33.2 ns (2%)	1.1	τ_1 = 5.5 ns (72%) τ_2 = 16.9 ns (25%) τ_3 = 54.1 ns (3%)	1.0	τ_1 = 1.9 ns (81%) τ_2 = 4.7 ns (17%) τ_3 = 18.1 ns (2%)	1.1
420 nm	τ_1 = 3.8 ns (79%) τ_2 = 10.2 ns (19%) τ_3 = 31.7 ns (2%)	1.0	τ_1 = 5.3 ns (76%) τ_2 = 16.5 ns (22%) τ_3 = 52.0 ns (2%)	1.0	τ_1 = 2.1 ns (88%) τ_2 = 5.5 ns (11%) τ_3 = 20.7 ns (1%)	1.1
450 nm	τ_1 = 3.8 ns (80%) τ_2 = 10.5 ns (18%) τ_3 = 33.6 ns (2%)	1.1	τ_1 = 5.4 ns (78%) τ_2 = 17.0 ns (20%) τ_3 = 54.5 ns (2%)	1.1	τ_1 = 2.2 ns (90%) τ_2 = 6.2 ns (9%) τ_3 = 23.5 ns (1%)	1.1

When the three objective compounds are doped in PMMA matrix with a weight ratio of 1%, the resultant film samples all show tri-exponential PL decay functions. For the **DP-TXO$_2$**-based film sample, its PL decay curves can be fitted with three lifetime components with τ_1 of ~ 4 ns, τ_2 of ~ 10 ns and τ_3 of 30-40 ns. Taking into consideration that in solution, the ^{1}CT state of **DP-TXO$_2$** shows much shorter lifetime than that of the ^{1}LE state, the excited state species with τ_1 of ~ 4 ns and τ_2 of ~ 10 ns in **DP-TXO$_2$**-based film sample is tentatively assigned to the ^{1}CT and ^{1}LE states, respectively. To verify this deduction, PL decay curves of the thin film sample at varied monitored λ_{em}s are recorded. As depicted in Figure S5 and Table S3, with increasing emission wavelength from 378 to 450 nm, the relative weight of the τ_1 component increases gradually from 68% to 80%, while that of the τ_2 component decreases commensurately from 29% to 18%. This variation trends on the relative weight of the shorter and longer lifetime components are consistent with the corresponding transient PL measurement results of **DP-TXO$_2$** in dilute BE solution, confirming the ^{1}CT and ^{1}LE characters of the τ_1 and τ_2 species, respectively. However, different from the solution samples, in 1wt.%-doped film sample of **DP-TXO$_2$**, a low-content excited state species with much longer life-time of τ_3 (30-40 ns) is observable at every monitored λ_{em}. Since the doping ratio of **DP-TXO$_2$** is as low as 1 wt.%, and at relatively high monitored PL energy (λ_{em} = 380-400 nm), the contribution from the intermolecular excimer species of **DP-TXO$_2$**, if present, should be negligible. Therefore, the emitting species with τ_3 of 30-40 ns in **DP-TXO$_2$** is tentatively assigned to delayed fluorescence (DF) originating from RISC processes.

With respect to **P-TXO$_2$** and **TPP-TXO$_2$**, their 1 wt.%-doped film samples also show tri-exponential PL decay functions. Consistent with their PL decay characters in dilute solutions, the τ_1 and τ_2 components of **P-TXO$_2$** both show longer lifetimes than those of **DP-TXO$_2$** (τ_1: 5 *vs* 4 ns; τ_2: 17 *vs* 10 ns); while the τ_1 and τ_2 components of **TPP-TXO$_2$** both show shorter lifetimes than those of **DP-TXO$_2$** (τ_1: 2 *vs* 4 ns; τ_2: 5 *vs* 10 ns). Similar to the **DP-TXO$_2$**-based film sample, a third species with longer lifetime of τ_3 than τ_1 and τ_2 is necessary to fit the PL decay functions of either **P-TXO$_2$**- or **TPP-TXO$_2$**-based sample. But in comparison with the **DP-TXO$_2$**-based film ($\tau_{3:}$ 30-40 ns), the lifetime of the third excited state species is much longer for the **P-TXO$_2$**-based sample ($\tau_{3:}$ 50-60 ns), and much shorter for the **TPP-TXO$_2$**-based sample ($\tau_{3:}$ < 25 ns).

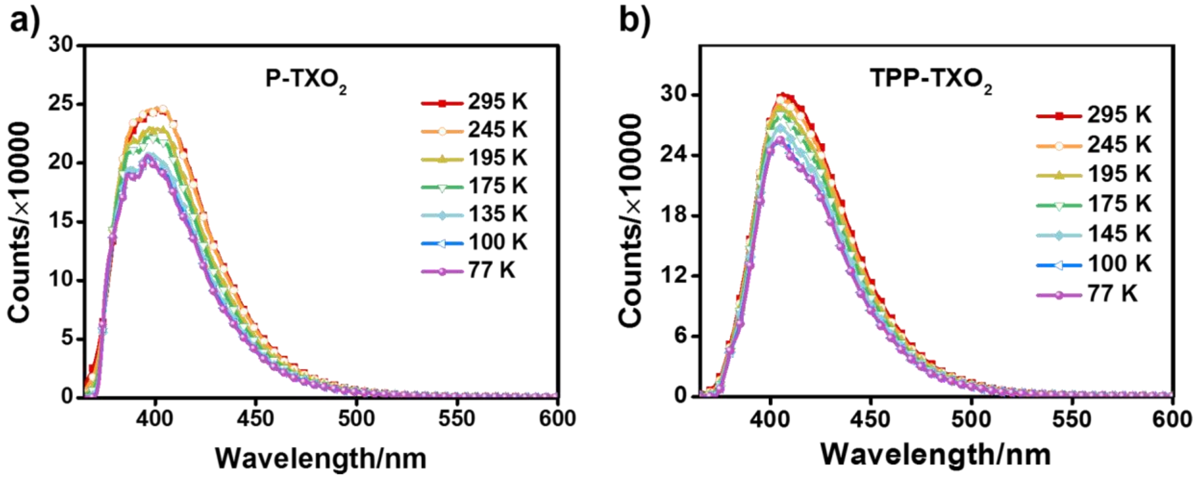

Figure S6. Temperature-dependent PL emission spectra of: a) **P-TXO$_2$**; and b) **TPP-TXO$_2$** in 1 wt.%-doped thin films in PMMA matrix at λ_{ex} of 350 nm.

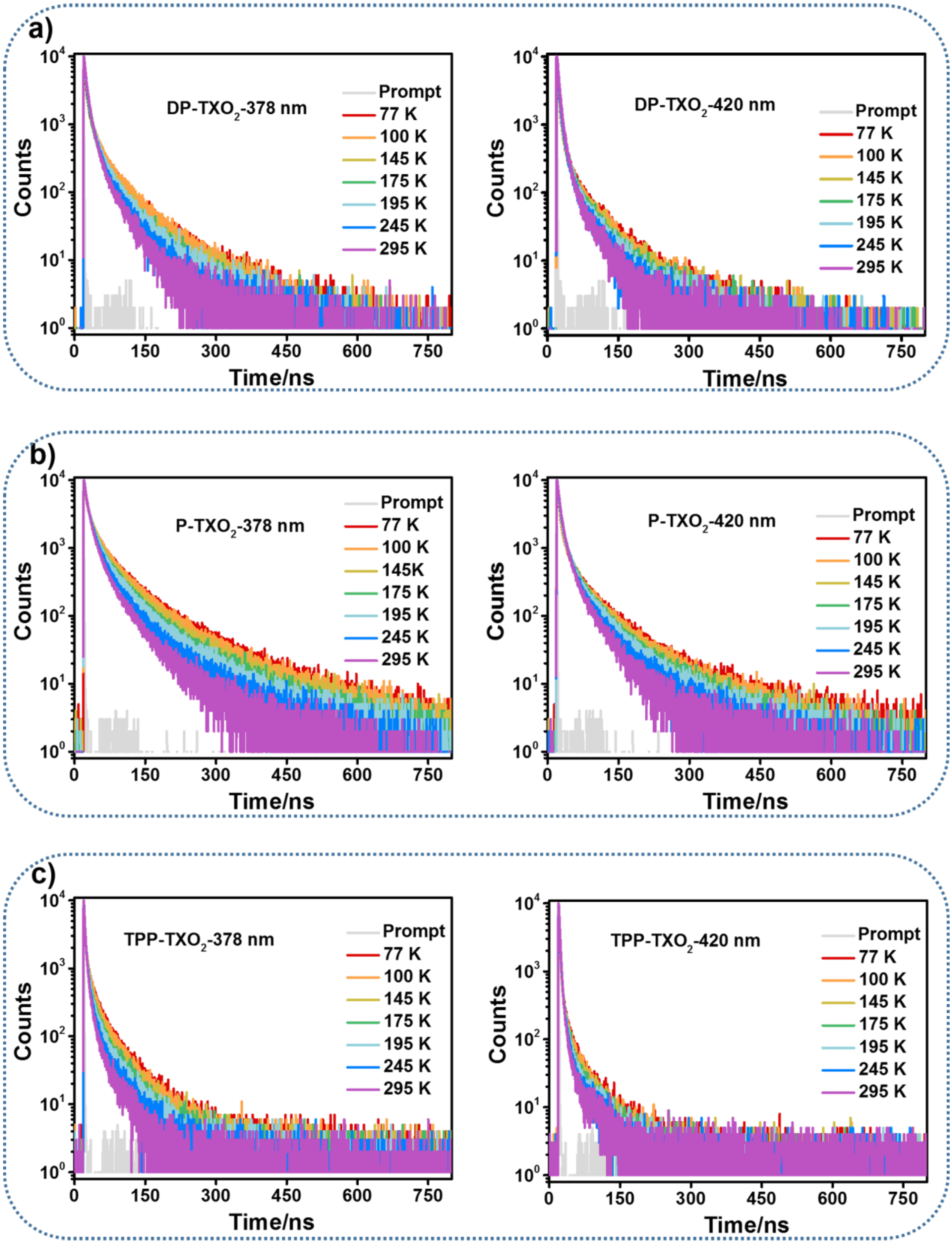

Figure S7. Temperature-dependent transient PL decay spectra of: a) **DP-TXO$_2$**; b) **P-TXO$_2$**; and b) **TPP-TXO$_2$** in doped films at λ_{em} of 378 nm and 420 nm (λ_{ex} = 320 nm).

Table S4. PL lifetimes of of the objective compounds in 1 wt.%-doped films in PMMA matrix at different temperatures.

		DP-TXO$_2$		**P-TXO$_2$**		**TPP-TXO$_2$**	
T	λ_{em}	lifetime (weight)	χ^2	lifetime (weight)	χ^2	lifetime (weight)	χ^2
295 K	378 nm	τ_1 = 4.1 ns (68%) τ_2 = 12.1 ns (29%) τ_3 = 40.6 ns (3%)	1.0	τ_1 = 5.6 ns (63%) τ_2 = 18.0 ns (33%) τ_3 = 59.2 ns (4%)	1.0	τ_1 = 1.7 ns (75%) τ_2 = 5.5 ns (23%) τ_3 = 23.2 ns (2%)	1.2
	400 nm	τ_1 = 3.8 ns (76%) τ_2 = 10.4 ns (22%) τ_3 = 33.2 ns (2%)	1.1	τ_1 = 5.5 ns (72%) τ_2 = 16.9 ns (25%) τ_3 = 54.1 ns (3%)	1.0	τ_1 = 1.9 ns (81%) τ_2 = 4.7 ns (17%) τ_3 = 18.1 ns (2%)	1.1
	420 nm	τ_1 = 3.8 ns (79%) τ_2 = 10.2 ns (19%) τ_3 = 31.7 ns (2%)	1.0	τ_1 = 5.3 ns (76%) τ_2 = 16.5 ns (22%) τ_3 = 52.0 ns (2%)	1.0	τ_1 = 2.1 ns (88%) τ_2 = 5.5 ns (11%) τ_3 = 20.7 ns (1%)	1.1
245 K	378 nm	τ_1 = 3.9 ns (72%) τ_2 = 13.2 ns (25%) τ_3 = 46.4 ns (3%)	1.1	τ_1 = 5.4 ns (65%) τ_2 = 20.2 ns (31%) τ_3 = 69.3 ns (4%)	1.1	τ_1 = 1.7 ns (77%) τ_2 = 6.0 ns (21%) τ_3 = 27.4 ns (2%)	1.2
	400 nm	τ_1 = 3.6 ns (82%) τ_2 = 11.6 ns (16%) τ_3 = 40.3 ns (2%)	1.0	τ_1 = 5.0 ns (74%) τ_2 = 18.1 ns (23%) τ_3 = 61.1 ns (3%)	1.2	τ_1 = 1.7 ns (83%) τ_2 = 4.8 ns (16%) τ_3 = 20.2 ns (1%)	1.0
	420 nm	τ_1 = 3.4 ns (82%) τ_2 = 9.9 ns (16%) τ_3 = 33.9 ns (2%)	1.0	τ_1 = 4.9 ns (77%) τ_2 = 17.4 ns (21%) τ_3 = 60.3 ns (2%)	1.1	τ_1 = 2.0 ns (90%) τ_2 = 6.5 ns (9%) τ_3 = 24.0 ns (1%)	1.1
195 K	378 nm	τ_1 = 3.6 ns (73%) τ_2 = 13.6 ns (24%) τ_3 = 52.0 ns (3%)	1.1	τ_1 = 5.5 ns (66%) τ_2 = 22.7 ns (29%) τ_3 = 76.8 ns (5%)	1.1	τ_1 = 1.7 ns (82%) τ_2 = 7.7 ns (16%) τ_3 = 33.6 ns (2%)	1.2
	400 nm	τ_1 = 3.4 ns (84%) τ_2 = 12.4 ns (14%) τ_3 = 46.3 ns (2%)	1.0	τ_1 = 4.7 ns (76%) τ_2 = 19.4 ns (21%) τ_3 = 69.5 ns (3%)	1.0	τ_1 = 1.7 ns (88%) τ_2 = 6.0 ns (11%) τ_3 = 27.5 ns (1%)	1.0
	420 nm	τ_1 = 3.3 ns (85%) τ_2 = 11.4 ns (13%) τ_3 = 41.8 ns (2%)	1.0	τ_1 = 4.6 ns (78%) τ_2 = 18.0 ns (19%) τ_3 = 66.3 ns (3%)	1.1	τ_1 = 1.9 ns (91%) τ_2 = 6.7 ns (8%) τ_3 = 27.7 ns (1%)	1.0
175 K	378 nm	τ_1 = 3.5 ns (78%) τ_2 = 13.8 ns (19%) τ_3 = 52.8 ns (3%)	1.1	τ_1 = 5.3 ns (66%) τ_2 = 22.7 ns (29%) τ_3 = 79.7 ns (5%)	1.1	τ_1 = 1.6 ns (81%) τ_2 = 7.3 ns (17%) τ_3 = 34.1 ns (2%)	1.2
	400 nm	τ_1 = 3.3 ns (85%) τ_2 = 12.5 ns (13%) τ_3 = 47.0 ns (2%)	1.1	τ_1 = 4.6 ns (77%) τ_2 = 20.1 ns (20%) τ_3 = 71.2 ns (3%)	1.1	τ_1 = 1.7 ns (91%) τ_2 = 7.1 ns (8%) τ_3 = 29.7 ns (1%)	1.0
	420 nm	τ_1 = 3.3 ns (86%) τ_2 = 11.7 ns (12%) τ_3 = 43.6 ns (2%)	1.0	τ_1 = 4.5 ns (80%) τ_2 = 19.3 ns (18%) τ_3 = 69.5 ns (2%)	1.0	τ_1 = 1.8 ns (92%) τ_2 = 6.9 ns (7%) τ_3 = 27.8 ns (1%)	1.1
145 K	378 nm	τ_1 = 3.3 ns (78%) τ_2 = 13.8 ns (19%) τ_3 = 56.0 ns (3%)	1.1	τ_1 = 5.3 ns (67%) τ_2 = 25.2 ns (28%) τ_3 = 87.9 ns (5%)	1.1	τ_1 = 1.5 ns (82%) τ_2 = 7.8 ns (15%) τ_3 = 36.4 ns (3%)	1.2
	400 nm	τ_1 = 3.2 ns (86%) τ_2 = 13.0 ns (12%) τ_3 = 52.0 ns (2%)	1.0	τ_1 = 4.4 ns (78%) τ_2 = 20.9 ns (18%) τ_3 = 76.3 ns (4%)	1.1	τ_1 = 1.7 ns (90%) τ_2 = 6.9 ns (9%) τ_3 = 29.9 ns (1%)	1.1
	420 nm	τ_1 = 3.1 ns (88%) τ_2 = 12.2 ns (11%) τ_3 = 48.0 ns (1%)	1.0	τ_1 = 4.3 ns (81%) τ_2 = 20.3 ns (16%) τ_3 = 75.7 ns (3%)	1.0	τ_1 = 1.7 ns (91%) τ_2 = 7.0 ns (8%) τ_3 = 29.9 ns (1%)	1.1
100 K	378 nm	τ_1 = 3.3 ns (78%) τ_2 = 15.5 ns (19%) τ_3 = 63.7 ns (3%)	1.1	τ_1 = 4.9 ns (67%) τ_2 = 26.9 ns (27%) τ_3 = 95.5 ns (6%)	1.2	τ_1 = 1.4 ns (83%) τ_2 = 8.6 ns (14%) τ_3 = 40.3 ns (3%)	1.3
	400 nm	τ_1 = 3.0 ns (87%) τ_2 = 14.1 ns (11%) τ_3 = 58.4 ns (2%)	1.0	τ_1 = 4.1 ns (80%) τ_2 = 22.4 ns (17%) τ_3 = 83.8 ns (3%)	1.1	τ_1 = 1.6 ns (91%) τ_2 = 7.5 ns (8%) τ_3 = 33.3 ns (1%)	1.1
	420 nm	τ_1 = 3.0 ns (88%) τ_2 = 12.4 ns (10%) τ_3 = 52.3 ns (2%)	1.0	τ_1 = 4.0 ns (83%) τ_2 = 21.2 ns (14%) τ_3 = 81.2 ns (3%)	1.1	τ_1 = 1.6 ns (91%) τ_2 = 6.7 ns (8%) τ_3 = 30.2 ns (1%)	1.1
77 K	378 nm	τ_1 = 3.1 ns (81%) τ_2 = 15.6 ns (16%) τ_3 = 65.3 ns (3%)	1.1	τ_1 = 4.7 ns (68%) τ_2 = 26.6 ns (26%) τ_3 = 97.5 ns (6%)	1.2	τ_1 = 1.4 ns (84%) τ_2 = 9.7 ns (13%) τ_3 = 43.8 ns (3%)	1.3
	400 nm	τ_1 = 3.0 ns (88%) τ_2 = 14.0 ns (10%) τ_3 = 60.3 ns (2%)	1.0	τ_1 = 4.0 ns (80%) τ_2 = 23.6 ns (16%) τ_3 = 90.0 ns (4%)	1.1	τ_1 = 1.5 ns (92%) τ_2 = 7.8 ns (7%) τ_3 = 34.6 ns (1%)	1.1
	420 nm	τ_1 = 2.9 ns (89%) τ_2 = 12.1 ns (10%) τ_3 = 54.8 ns (1%)	1.0	τ_1 = 3.9 ns (84%) τ_2 = 21.6 ns (14%) τ_3 = 86.4 ns (2%)	1.1	τ_1 = 1.6 ns (92%) τ_2 = 7.8 ns (7%) τ_3 = 34.3 ns (1%)	1.1

For all the three 1 wt.%-doped films, with decreasing temperature from 295 K to 77 K, the PL intensity is found to decrease gradually, implying their decreased φ_{PL} values upon cooling down. Taking into account that in Hex, the $\varphi_{PL(LE)}$ and $\varphi_{PL(CT)}$ of **DP-TXO$_2$** are comparable, the decreased φ_{PL} of the samples upon cooling down should not mainly originate from the alteration in the contribution from their ^{1}CT and ^{1}LE states, but from the reduced contribution from their DF components. This deduction is further confirmed by the transient PL characterization results, since for all the three compounds, their τ_3 species with the longest lifetime are observed to be prolonged upon cooling down, suggesting that the τ_3 species in all the three compounds show a thermo-activated feature. Meanwhile, at 77 K, all these samples show more structured PL spectra than those recorded at 295 K, whcih should be ascribed to the less polar environments of these compounds in 77 K than 295 K.

Among all the three objective compounds, **TPP-TXO$_2$** possesses a τ_3 species with the shortest lifetime. Accordingly, the RISC processes in **TPP-TXO$_2$** should be faster than those in **DP-TXO$_2$** and **P-TXO$_2$**. In fact, even in 77 K and 100 K, the lifetime of the τ_3 species of **TPP-TXO$_2$** is as short as cal. 35 ns, indicative of the presence of relatively fast RISC processes even at a rather low-temperature of 77 K. Therefore, upon cooling down from 295 K to 77 K, the **TPP-TXO$_2$**-based sample shows the smallest PL intensity depression among the three samples.

Table S5. Summary of the transition characters of the objective compounds calculated from the photophysical data of the 1 wt.%-doped PMMA films (λ_{em} = 400 nm, 295 K).

Compd.	τ_1/[ns] (α_1)	τ_2/[ns] (α_2)	τ_3/[ns] (α_3)	τ_p/[ns] (α_p)	τ_d/[ns] (α_d)	φ_{PL}	φ_p	φ_d	k_p/[s^{-1}]	k_d/[s^{-1}]	k_r^S/[s^{-1}]	k_{ISC}/[s^{-1}]	k_{RISC}/[s^{-1}]
DP-TXO$_2$	3.8(0.76)	10.4(0.22)	33.2(0.02)	5.2(0.98)	33.2(0.02)	0.48	0.42	0.06	1.9×10^8	3.0×10^7	8.1×10^7	11.1×10^7	7.3×10^6
P-TXO$_2$	5.5(0.72)	16.9(0.25)	54.4(0.03)	8.2(0.97)	54.1(0.03)	0.48	0.40	0.08	1.2×10^8	1.8×10^7	4.9×10^7	7.4×10^7	5.8×10^6
TPP-TXO$_2$	1.9(0.81)	4.7(0.17)	18.1(0.02)	2.3(0.98)	18.1(0.02)	0.47	0.41	0.06	4.3×10^8	5.5×10^7	17.8×10^7	25.6×10^7	13.5×10^6

τ: fitted lifetime;
τ_p and τ_d: lifetimes of the prompt fluorescence and delayed fluorescence, respectively;
φ_{PL}: absolute PL quantum yield of the sample measured in an intergrating sphere;
φ_p and φ_d: PL quantum yields of the prompt fluorescence and delayed fluorescence, respectively;
α: fitted pre-exponential factor of the fluorescence species;
α_p and α_d: fitted pre-exponential factors of the prompt fluorescence and delayed fluorescence species, respectively;
k_p: deactiviation rate constant of the excited singlet state formed directly upon excitation;
k_d: deactiviation rate constant of the excited triplet state;
k_r^S: radiative decay rate constant of the singlet excited state in the prompt fluorescence process;
k_{ISC}: intersystem crossing rate constant from excited singlet to triplet state;
k_{RISC}: rate constant of the reverse intersystem crossing process from excited triplet to singlet state.[4]

The PL decay curves of all these 1 wt.%-doped film samples are observed to show tri-exponential functions with lifetimes of τ_1, τ_2 and τ_3, respectively (vide Table S5). As discussed earlier, the two species with shorter lifetime of τ_1 and τ_2 should be assigned to the ^{1}CT and ^{1}LE states, respectively, and the component with much longer lifetime of τ_3 should be assigned to the DF, the weighted average lifetimes of the τ_1 and τ_2 species of these samples are used as the τ_p of their prompt fluorescence decay, and the lifetimes of the τ_3 components are used as the τ_d of their delayed fluorescence decay, as depicted in the following formulas (2) and (3). Accordingly, the τ_p values of **DP-TXO$_2$**-, **P-XO$_2$**- and **TPP-TXO$_2$**-based samples are 5.2 ns, 8.2 ns and 2.3 ns, respectively; and the corresponding τ_d values are 33.2 ns, 54.1 ns and 18.1 ns, in sequence. Consequently, according to equations (4) and (5), the k_ps of **DP-TXO$_2$**, **P-XO$_2$** and **TPP-TXO$_2$** are calculated to be 1.9×10^8, 1.2×10^8 and 4.3×10^8 s^{-1}, respectively; and the k_ds of **DP-TXO$_2$**, **P-XO$_2$** and **TPP-TXO$_2$** are calculated to be 3.0×10^7, 1.8×10^7 and 5.5×10^7 s^{-1}, respectively.

$$\tau_p = \tau_1\alpha_1 + \tau_2\alpha_2 \qquad (2)^{[4a]}$$

$$\tau_d = \tau_3 \qquad (3)$$

$$k_{\mathrm{p}} = \frac{1}{\tau_{\mathrm{p}}} \tag{4}$$ [4e]

$$k_{\mathrm{d}} = \frac{1}{\tau_{\mathrm{d}}} \tag{5}$$ [4e]

Since the fractional (f) or relative amplitude of each fluorescing component is expressed as equation (6), the contributions from the prompt (φ_{P}) and delayed fluorescence (φ_{d}) to the whole φ_{PL} of the samples can be calculated according to equations (7) and (8). The results indicate that the corresponding φ_{p} data for all the compounds are ~ 0.4, and the φ_{d} values of all these compounds are 0.06-0.08.

$$f = \frac{\alpha_{\mathrm{i}}\tau_{\mathrm{i}}}{\sum\alpha_{\mathrm{i}}\tau_{\mathrm{i}}} \tag{6}$$ [4b]

$$\varphi_{\mathrm{p}} = \frac{\alpha_{\mathrm{p}}\tau_{\mathrm{p}}}{\alpha_{\mathrm{p}}\tau_{\mathrm{p}}+\alpha_{\mathrm{d}}\tau_{\mathrm{d}}}\varphi_{\mathrm{PL}} \tag{7}$$ [4b]

$$\varphi_{\mathrm{d}} = \frac{\alpha_{\mathrm{d}}\tau_{\mathrm{d}}}{\alpha_{\mathrm{p}}\tau_{\mathrm{p}}+\alpha_{\mathrm{d}}\tau_{\mathrm{d}}}\varphi_{\mathrm{PL}} \tag{8}$$ [4b]

Because the interal conversion rate constant ($k_{\mathrm{IC}}^{\mathrm{S}}$) of pyrene was reported to be as small as 5.9×10^{5} s^{-1},[5] and all the objective compounds possess a rather large band-gap (E_{g}) of > 3 eV, relatively small $k_{\mathrm{Ic}}^{\mathrm{S}}$ values of the objective compounds can be expected. Therefore, functional relationships between the rate constants of $k_{\mathrm{r}}^{\mathrm{S}}$ and k_{ISC} can be expressed as equation (9). As according to equation (10), the $k_{\mathrm{r}}^{\mathrm{S}}$ values of **DP-TXO$_2$**, **P-XO$_2$** and **TPP-TXO$_2$** are calculated to be 8.1×10^{7}, 4.9×10^{7} and 17.8×10^{7} s^{-1}, respectively, the k_{ISC} values of **DP-TXO$_2$**, **P-XO$_2$** and **TPP-TXO$_2$** are determined to be 11.1×10^{7}, 7.4×10^{7} and 25.6×10^{7} s^{-1}, respectively.

$$\varphi_{\mathrm{p}} = \frac{k_{\mathrm{r}}^{\mathrm{S}}}{k_{\mathrm{r}}^{\mathrm{S}}+k_{\mathrm{ISC}}} \tag{9}$$

$$k_{\mathrm{r}}^{\mathrm{S}} = \frac{\varphi_{\mathrm{p}}}{\tau_{\mathrm{p}}} \tag{10}$$ [4c-4e]

As the φ_{p} values of these compounds are ~ 0.4, their $k_{\mathrm{r}}^{\mathrm{S}}$ and k_{ISC} values should be of the same order of magnitudes; as the φ_{d} values of these compounds are 0.06-0.08, it can be assumed that $k_{\mathrm{r}}^{\mathrm{S}}$, $k_{\mathrm{ISC}} > k_{\mathrm{RISC}}$, i.e., the RISC process should be the rate-controling step because of the smaller k_{RISC}. Under these conditions, the functional relationship of these rate constants can be expressed as equation (11):

$$k_{\mathrm{RISC}} = \frac{k_{\mathrm{d}} k_{\mathrm{p}} \varphi_{\mathrm{d}}}{k_{\mathrm{ISC}} \varphi_{\mathrm{p}}} \qquad (11)^{[4c\text{-}4e]}$$

Accordingly, the k_{RISC}s of **DP-TXO$_2$**, **P-XO$_2$** and **TPP-TXO$_2$** are determined to be 7.3 $\times 10^6$ s^{-1}, 5.8 $\times 10^6$ s^{-1} and 13.5 $\times 10^6$ s^{-1} in sequence. Note that among the three compounds, **TPP-TXO$_2$** displays the largest $k_{\mathrm{r}}^{\mathrm{S}}$, k_{ISC} as well as k_{RISC}, which are quite beneficial to the triplet exciton harvesting in OLED applications.

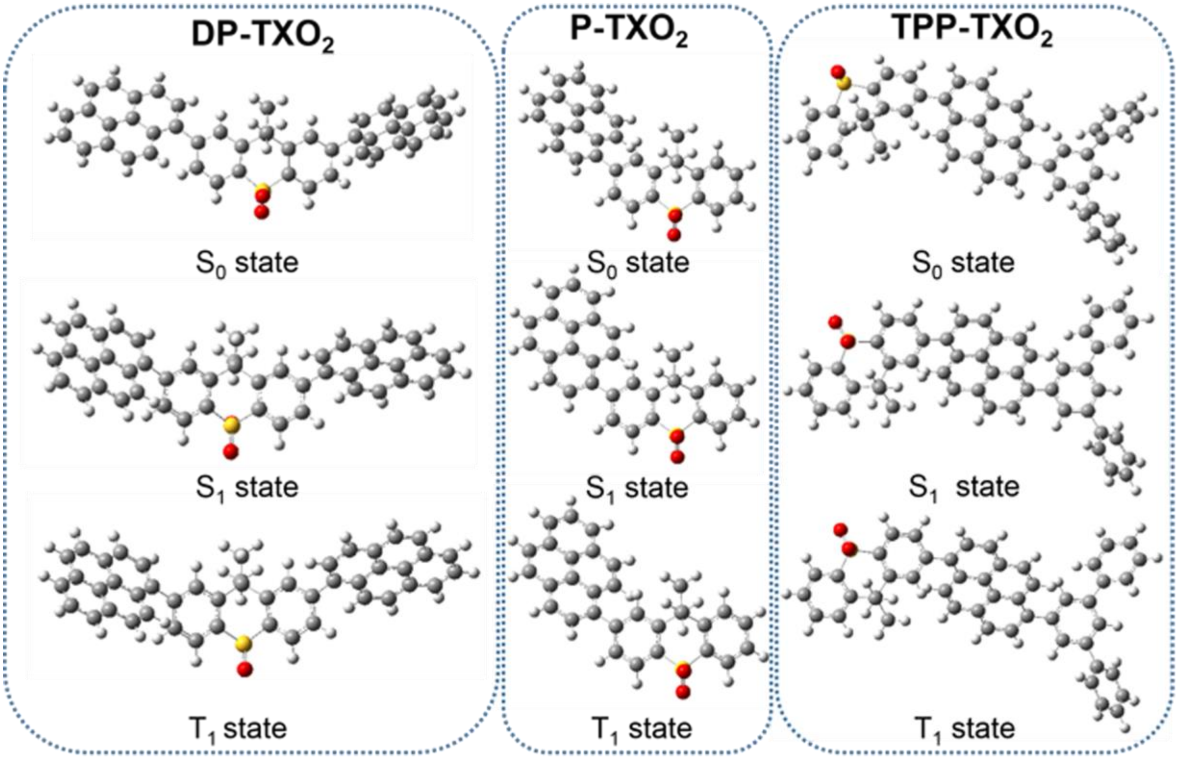

Figure S8. Optimized ground state (S$_0$ state) and excited state (S$_1$ and T$_1$ states) geometries of a) **DP-TXO$_2$**; b) **P-TXO$_2$**; and c) **TPP-TXO$_2$**.

Table S6. Comparion of calculated geometry parameters of **DP-TXO$_2$** with the corresponding experimental findings (derived from crystallographic analysis).

Bond lengths	Experimental	Calculated	Bond/Torsion angles	Experimental	Calculated
S01-O002	1.434(3)	1.466	O002-S01-C008	109.4(9)	109.0
S01-O003	1.435(3)	1.470	O003-S01-O002	117.4(9)	118.4
S01-C008	1.752(3)	1.790	C00A-C004-C00H	120.2(3)	120.3
C004-C00A	1.421(4)	1.430	C00B-C005-C006	115.6(3)	115.9
C005-C006	1.400(4)	1.399	C009-C006-C005	122.7(3)	122.9
C006-C009	1.395(4)	1.402	C00I-C008-S01	116.0(2)	116.8
C009-C00P	1.396(5)	1.399	C00P-C009-C006	119.1(3)	118.9
C00B-C00M	1.393(4)	1.392	C00K-C00D-C008	115.6(3)	115.9
C00C-C00Y	1.438(5)	1.435	C00J-C00E-C007	121.9(3)	121.8
C00D-C00K	1.401(4)	1.399	C005-C00F-C013	107.5(3)	109.0
C00E-C00J	1.380(5)	1.387	C017-C00F-C013	109.1(4)	106.6
C00F-C017	1.539(5)	1.541	C00N-C00I-C008	119.3(3)	119.7
C00G-C00N	1.392(5)	1.399	C00Z-C00O-C00G	118.4(3)	118.5
C00H-C00W	1.425(6)	1.425	C00S-C00Q-C015	119.7(4)	119.5
C00I-C00N	1.370(5)	1.387	C00Q-C00S-C011	118.6(3)	118.3
C00L-C00Q	1.430(5)	1.430	C01B-C01D-C015	121.1(4)	120.8
C00M-C00P	1.373(5)	1.387	O002-S01-C008-C00I	36.5(2)	31.5
C00O-C00R	1.408(5)	1.417	C008-C00I-C00N-C00G	-1.1(2)	0.9
C00Q-C00S	1.411(6)	1.425	C00Z-C00O-C00G-C00N	-128.9(1)	-121.7
C00R-C00X	1.439(5)	1.438	C013-S01-C008-C00I	152.1(1)	145.5
C00S-C016	1.405(6)	1.402	C00X-C00R-C00O-C00G	8.4(2)	4.3
C00T-C01C	1.412(6)	1.402	C00Z-C00O-C00G-C00K	48.5(2)	55.3
C00U-C014	1.356(5)	1.359	C006-C009-C007-C00E	49.5(2)	58.0
C00V-C018	1.438(5)	1.435	C017-C00F-C005-C006	30.0(1)	16.7
C00W-C014	1.413(6)	1.433	C00P-C009-C007-C00A	53.5(3)	59.1
C00X-C011	1.348(5)	1.359	C013-C00F-C005-C006	-88.7(5)	-100.2
C00Y-C012	1.334(6)	1.358	C009-C007-C00E-C00J	175.8(7)	178.3
C00Z-C010	1.381(5)	1.387	C00F-C005-C00B-C00M	-177.7(3)	-179.6
C019-C01E	1.368(8)	1.391	C00K-C00D-C008-S01	-170.6(6)	-179.0
C01B-C01D	1.384(9)	1.391	C00K-C00G-C00N-C00I	2.9(2)	0.4

Table S7. Comparion of calculated geometry parameters of **P-TXO₂** with the corresponding experimental findings (derived from crystallographic analysis).

Bond lengths	Experimental	Calculated	Bond/Torsion angles	Experimental	Calculated
S1-O1	1.437(2)	1.480	O1-S1-C1	108.8(5)	108.9
S1-O2	1.434(2)	1.466	O1-S1-C13	107.2(3)	108.9
S1-C1	1.751(3)	1.792	C2-C1-S1	115.4(7)	116.5
S1-C13	1.743(2)	1.790	C2-C1-C6	123.3(2)	123.2
C1-C2	1.392(3)	1.392	C1-C2-C3	119.1(3)	119.4
C2-C3	1.384(4)	1.389	C8-C7-C6	114.5(3)	110.6
C3-C4	1.369(4)	1.391	C14-C7-C15	110.2(2)	106.6
C4-C5	1.376(4)	1.394	C9-C8-C7	120.0(2)	122.0
C5-C6	1.404(3)	1.401	C9-C10-C16	121.9(2)	120.7
C6-C7	1.537(3	1.546	C29-C16-C17	119.1(2)	119.2
C7-C8	1.537(3)	1.546	C19-C18-C17	122.0(3)	121.7
C8-C9	1.399(3)	1.399	C18-C19-C20	120.9(3)	121.6
C9-C10	1.397(3)	1.403	C22-C23-C24	121.7(4)	120.9
C10-C11	1.392(4)	1.398	C25-C24-C31	118.9(3)	118.7
C11-C12	1.369(4)	1.388	C26-C25-C24	121.8(3)	121.2
C12-C13	1.389(3)	1.391	S1-C1-C2-C3	-176.2(2)	-178.4
C16-C17	1.411(4)	1.416	S1-C1-C6-C5	175.8(2)	179.1
C17-C18	1.440(4)	1.439	O1-S1-C1-C2	89.3(2)	99.0
C18-C19	1.356(4)	1.359	O1-S1-C13-C8	83.7(2)	80.8
C19-C20	1.426(4)	1.433	O2-S1-C13-C12	39.2(2)	32.3
C20-C21	1.400(4)	1.402	C1-S1-C13-C8	-31.3(2)	-34.2
C21-C22	1.375(5)	1.391	C2-C1-C6-C7	-178.2(2)	-179.4
C22-C23	1.369(6)	1.391	C3-C4-C5-C6	0.2(5)	0.8
C23-C24	1.401(5)	1.402	C4-C5-C6-C1	0.8(4)	-0.5
C24-C25	1.415(5)	1.435	C5-C6-C7-C8	160.6(2)	140.7
C25-C26	1.352(5)	1.358	C9-C8-C13-S1	-166.4(5)	-179.4
C26-C27	1.439(4)	1.435	C8-C9-C10-C11	-0.2(4)	-0.6
C27-C28	1.383(4)	1.400	C11-C10-C16-C29	46.9(4)	58.2
C28-C29	1.381(4)	1.387	C29-C16-C17-C30	0.6(4)	1.8
C30-C31	1.419(4)	1.427	C31-C20-C21-C22	-0.2(5)	0.0

DP-TXO$_2$

	Hole		Particle	Transition Character	ΔE (*f*)	ΔE$_{exp.}$
S$_0$-S$_1$		93.8% →	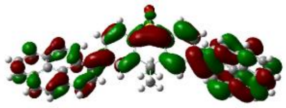	HLCT	3.28 eV (1.03)	3.28 eV
S$_0$-S$_2$	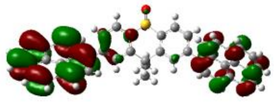	96.6% →	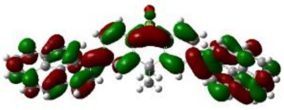	HLCT	3.35 eV (0.08)	-
S$_0$-T$_1$	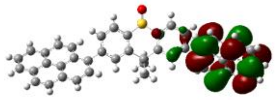	95.2% →	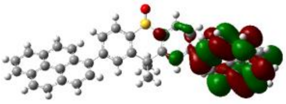	LE	2.08 eV (0.00)	2.07 eV
S$_0$-T$_2$		94.1% →	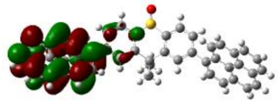	LE	2.19 eV (0.00)	-
S$_0$-T$_3$		62.3% →	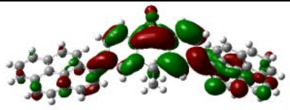	LE-dominated	3.26 eV (0.00)	-
	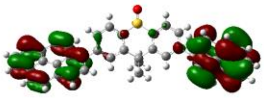	20.0% →		LE		
S$_0$-T$_4$	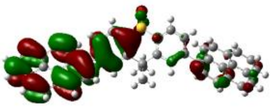	55.8% →		LE-dominated	3.31 eV (0.00)	-
		18.8% →		LE		
		12.5% →		LE		
S$_0$-T$_5$	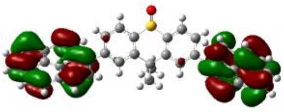	48.9% →	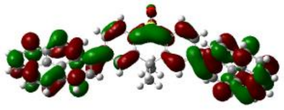	HLCT	3.43 eV (0.00)	-
		47.9% →		LE		

Figure S9. Calculated natural transition orbital (NTO) pairs and energy levels of the excited singlet and triplet states of **DP-TXO$_2$** in Hex.

Owing to its symmetrical D-A-D structure, **DP-TXO$_2$** is calculated to show pseudo-degenerated S$_1$ and S$_2$ states whose bandgaps are ~3.3 eV, T$_1$ and T$_2$ states whose bandgaps are ~2.1 eV, and T_3 and T_4 states whose bandgaps are ~3.3 eV, as shown in Figure S9. Note that the calculated energy gap of S_1/S_2 and T_1/T_2 states are quite similar to the experimental findings of **DP-TXO$_2$** derived from the onset of its absorption spectrum in Hex at 295 K and the higher-energy vibrational peak of its phosphorescence spectrum in 2-Me-THF at 77K, suggesting that the calculation results are reliable.

For the S_1 and S_2 states, their NTO hole wavefunctions both mainly distribute on the pyrene segments and partially delocalized in their adjacent phenyl rings of the TXO$_2$ segment; and their NTO particle wavefunctions are both found to locate in the whole molecule. Therefore, both the S_1 and S_2 states of **DP-TXO$_2$** show HLCT state character. For the T_1 and T_2 states, their NTO hole and particle wavefunctions are calculated to be mainly comfined on the pyrene subunits with a slight distribution on their adjacent phenyl rings of the TXO$_2$ segment, demonstrating a pyrene-centered LE character. As the energy gap (ΔE) between the S_1/S_2 and T_1/T_2 is as large as 1.2 eV, no significant RISC should occure between them. Nonetheless, the higher-lying T_3 and T_4 states of **DP-TXO$_2$** are calculated to show quite similar energy levels to those of S_1 and S_2 states (ΔE_{ST}: 0.02 ~ 0.09 eV). In addition to the relatively small ΔE_{ST}, both the T_3 and T_4 states are calculated to possess LE-dominated feature locating in either the whole molecule or the pyrene segments. As the S_1/S_2 and T_3/T_4 states show marked difference in the nature of these excited states, and the ΔE_{ST} between them is relatively small, relatively large spin-orbital coupling (SOC) elements between the S_1/S_2 and T_3/T_4 states could be expected,[4a] leading to relatively rapid ISC/RISC processes between them hence relatively large k_{ISC} and k_{RISC} of **DP-TXO$_2$**. Furthermore, the ΔE between the T_3/T_4 and T_1/T_2 states are quite large (> 1.0 eV), which is propitious to the significant decreasing of the k_{IC} from T_3/T_4 to T_1/T_2 according to the energy-gap law.[6] As a consequence, more-competitive RISC processes than IC processes could be expected in **DP-TXO$_2$** due to the greatly enhanced k_{RISC} owing to the small ΔE_{ST} together with relatively large SOC elements between the T_3/T_4 and S_1/S_2, and the large ΔE between the T_3/T_4 and T_1/T_2 states of **DP-TXO$_2$**.

P-TXO$_2$					
	Hole	Particle	Transition Character	ΔE (f)	$\Delta E_{\text{exp.}}$
S_0-S_1	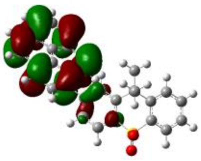 97.0% →	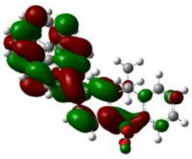	HLCT	3.39 eV (0.54)	3.30 eV
S_0-T_1	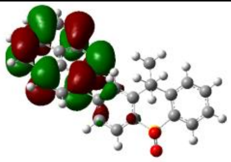 94.5% →	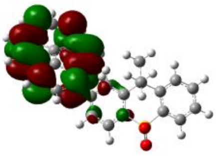	LE	2.11 eV (0.00)	2.09 eV
S_0-T_2	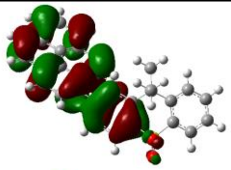 68.2% →	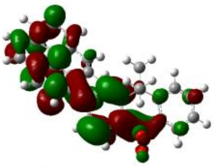	LE-dominated	3.29 eV (0.00)	-
	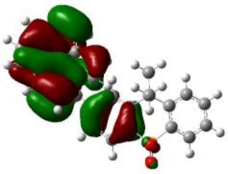 22.5% →	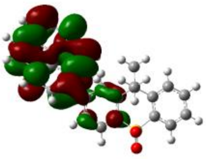	LE		
S_0-T_3	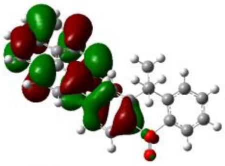 64.5% →	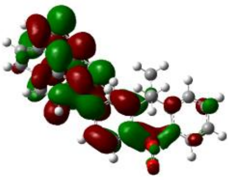	LE-dominated	3.45 eV (0.00)	-
	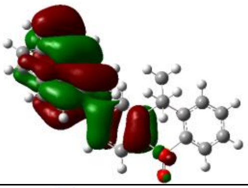 21.7% →	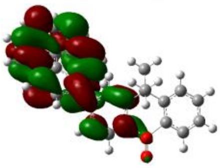	LE		
S_0-T_4	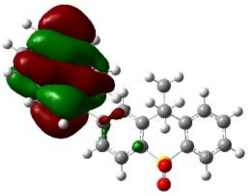 65.0% →	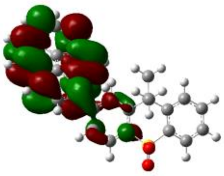	LE-dominated	3.52 eV (0.00)	-
	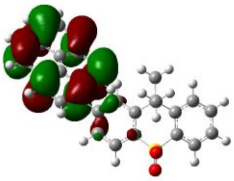 33.4% →	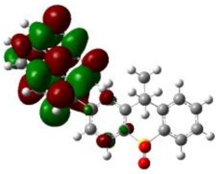	LE		

Figure S10. Calculated natural transition orbital (NTO) pairs and energy levels for the excited singlet and triplet states of **P-TXO$_2$** in Hex.

With respect to **P-TXO$_2$**, the energy levels of its S$_1$, T$_1$ and T$_2$ states are calculated to be 3.39 eV, 2.11 eV and 3.29 eV, respectively (vide Figure S10). The enengy levels of the calculated S$_1$ and T$_1$ states of **P-TXO$_2$** are in accordance with the corresponding experimental findings. Similar to the computing results results of **DP-TXO$_2$**, the S$_1$, T$_1$ and T$_2$ states of **P-TXO$_2$** are calculated to show HLCT, LE-dominated and LE-dominated characters, respectively. Although the $\Delta E_{(S1\text{-}T1)}$ of **P-TXO$_2$** is as large as 1.28 eV, the $\Delta E_{(S1\text{-}T2)}$ of **P-TXO$_2$** is much smaller (0.1 eV). Similar to **DP-TXO$_2$**, the marked difference in the nature of the S$_1$ and T$_2$ states of **P-TXO$_2$** together with a relatively small ΔE_{ST} between them will lead to relatively large spin-orbital coupling (SOC) elements between the S$_1$ and T$_2$ states of **P-TXO$_2$**, leading to relatively rapid ISC/RISC processes between them hence relatively large k_{ISC} and k_{RISC} of **P-TXO$_2$**. In addition, the ΔE between the T$_2$ and T$_1$ states of **P-TXO$_2$** are also quite large (1.18 eV), which is propitious to the significant decreasing of the k_{IC} from T$_2$ to T$_1$ states. Therefore, **P-TXO$_2$** also possesses more-competitive RISC processes than IC processes.

However, in comparison with that of **DP-TXO$_2$**, the $\Delta E_{(S1\text{-}T2)}$ of **P-TXO$_2$** is slightly higher (0.1 vs 0.02 eV), which is adverse to the efficient RISC processes from T$_2$ state to S$_1$ state. This may account for the smaller k_{ISC} and k_{RISC} of **P-TXO$_2$** than those of **DP-TXO$_2$**.

TPP-TXO$_2$						
	Hole		Particle	Transition Character	Δ*E*(*f*)	Δ*E*$_{exp.}$
S_0-S_1	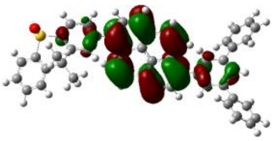	97.1%		HLCT	3.23 eV (0.86)	3.16 eV
S_0-T_1	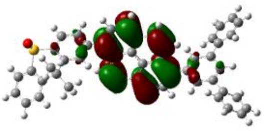	94.9%	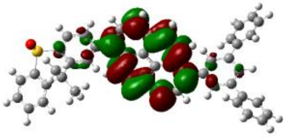	LE	2.04 eV (0.00)	2.04 eV
S_0-T_2	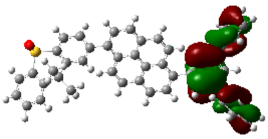	53.2%	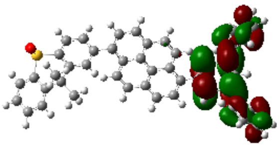	LE	3.19 eV (0.00)	-
	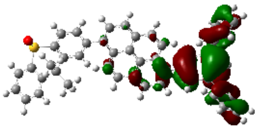	32.1%	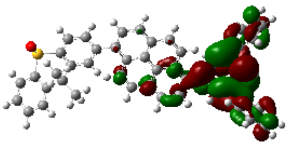	LE		
S_0-T_3	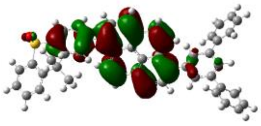	72.1%	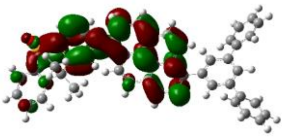	LE-dominated	3.28 eV (0.00)	-
	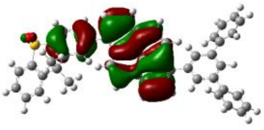	20.3%	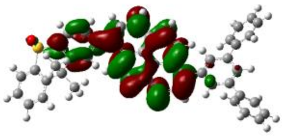	LE		
S_0-T_4	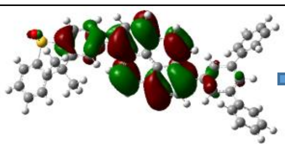	67.5%	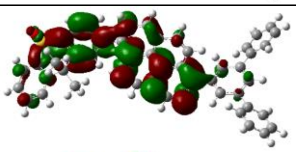	LE-dominated	3.39 eV (0.00)	-
	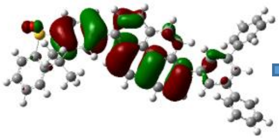	15.7%	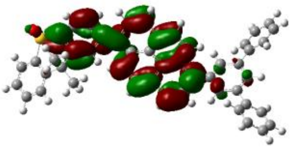	LE		

Figure S11. Calculated natural transition orbital (NTO) pairs and energy levels for the excited singlet and triplet states of **TPP-TXO$_2$** in Hex.

In the case of **TPP-TXO$_2$**, the energy levels of its S_1, T_1, T_2, and T_3 states are calculated to be 3.23 eV, 2.04 eV, 3.19 eV, and 3.28 eV in sqeuence (vide Figure S11). Similar to the computing results of **DP-TXO$_2$** and **P-TXO$_2$**, the S_1 and T_1 states of **TPP-TXO$_2$** are calculated to show HLCT and LE-dominated (mainly on the pyrene subunit) characters, respectively, and the $\Delta E_{(S1\text{-}T1)}$ of **TPP-TXO$_2$** is 1.2 eV. It should be pointed out that for both the S_1 and T_1 states of **TPP-TXO$_2$**, distinct contribution from the phenyl substituent grafted at the 6-site of the pyrene unit could be observed. Therefore, the slightly narrowed singlet and triplet energy bandgaps of **TPP-TXO$_2$** than **DP-TXO$_2$** and **P-TXO$_2$** should be attibuted to its more extended conjugation system to the 6-phenyl substituent. However, for the T_2 state, both its NTO hole and particle wavefunctions are mainly confined on the terphenyl substituent at the pyrene unit, leading to a LE-dominated character. Taking into consideration that the $\Delta E_{(S1\text{-}T2)}$ of **TPP-TXO$_2$** is as small as 0.04 eV, and the S_1 and T_2 states show marked difference in the nature of these excited states, much larger SOC element between the S_1 and T_2 states can be expected in **TPP-TXO$_2$** than **DP-TXO$_2$** and **P-TXO$_2$**,[4a] leading to the shortest lifetime of the DF and the largest k_{ISC} and k_{RISC} among the three objective compounds.

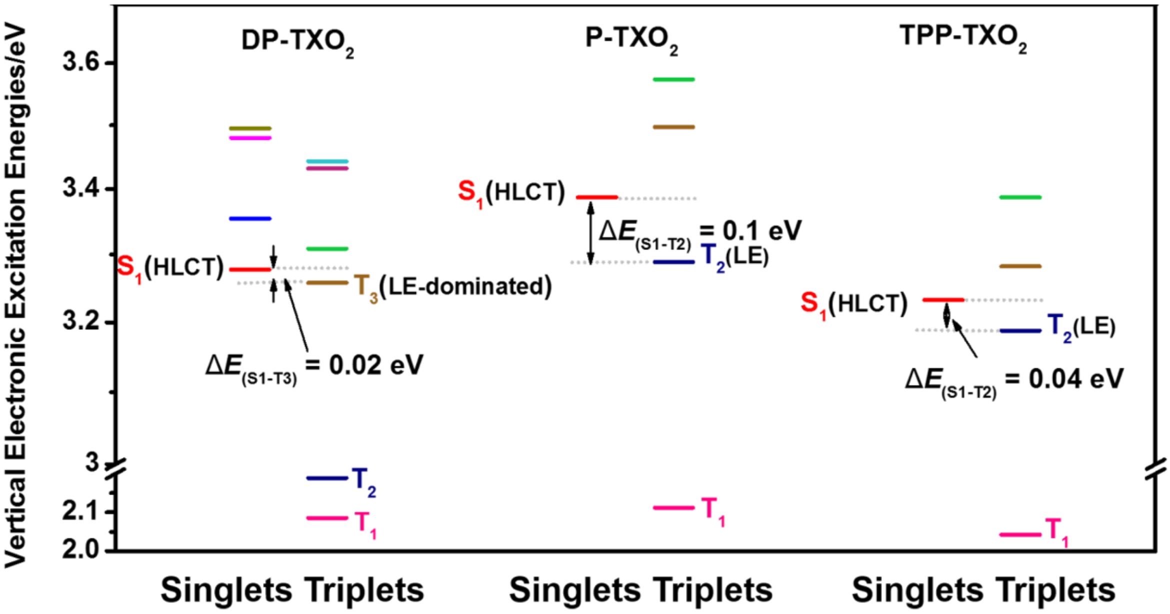

Figure S12. The calculated energy-level diagram of the excited singlet and triplet states of **DP-TXO$_2$**, **P-TXO$_2$** and **TPP-TXO$_2$**.

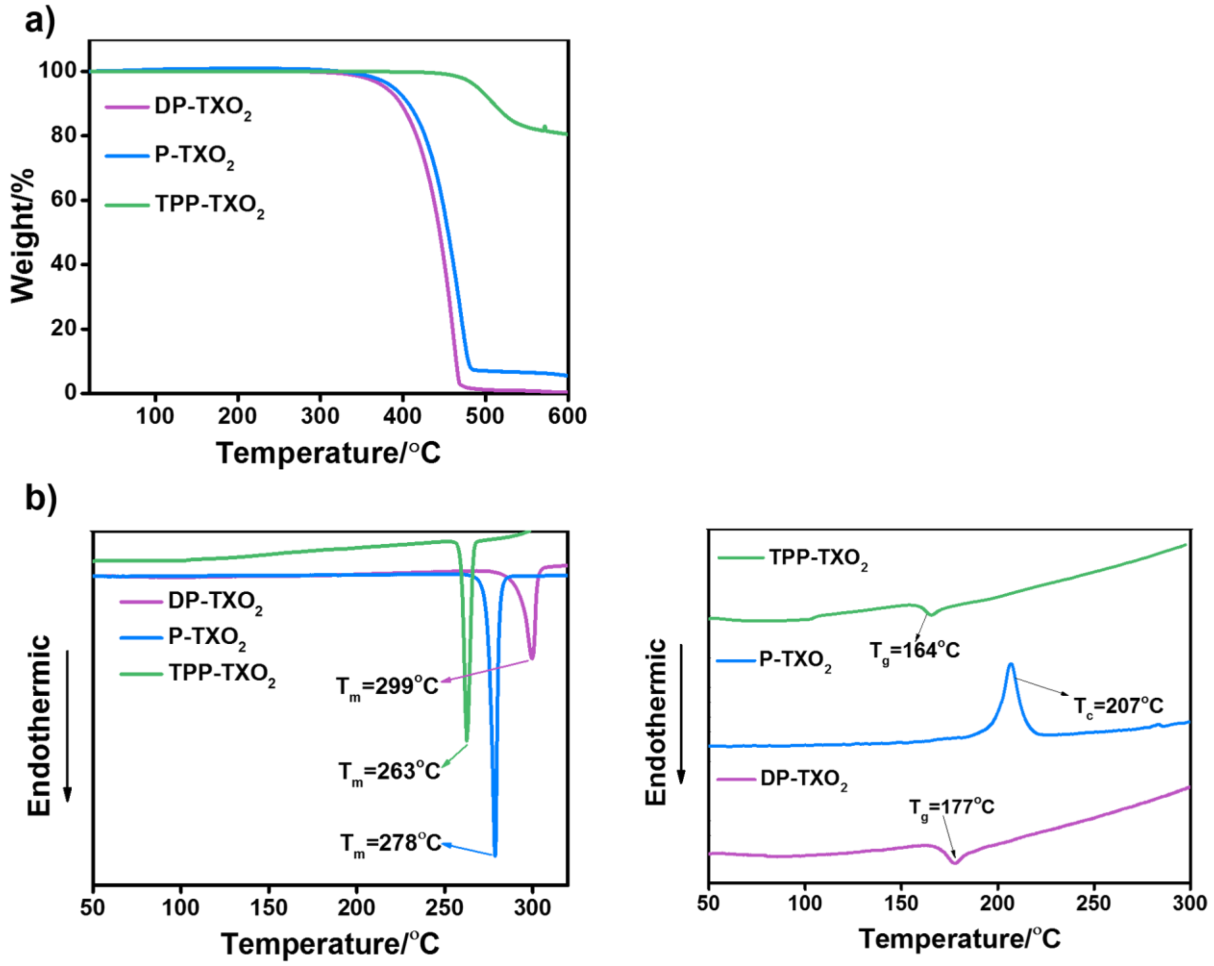

Figure S13. a) TGA thermograms of **DP-TXO$_2$**, **P-TXO$_2$** and **TPP-TXO$_2$**; b) DSC thermograms of **DP-TXO$_2$**, **P-TXO$_2$** and **TPP-TXO$_2$**.

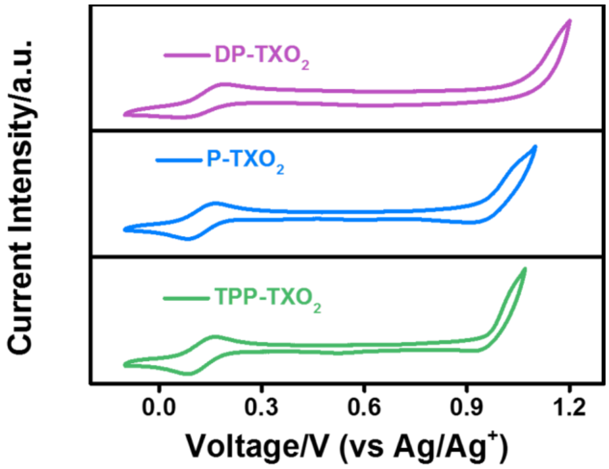

Figure S14. Cyclic voltammograms of **DP-TXO$_2$**, **P-TXO$_2$** and **TPP-TXO$_2$**.

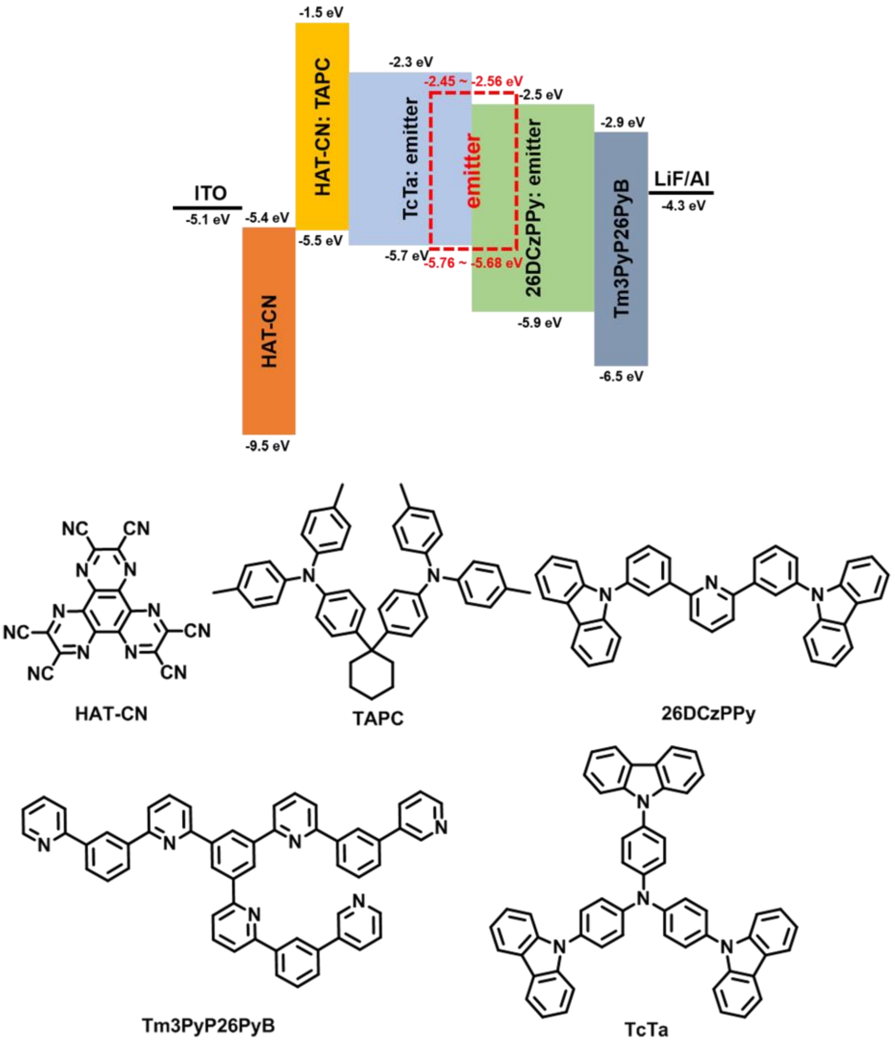

Figure S15. Device configuration and energy-level diagram of the OLEDs, and the molecular structures of HAT-CN, TAPC, TcTa, 26DCzPPy and Tm3PyP26PyB.

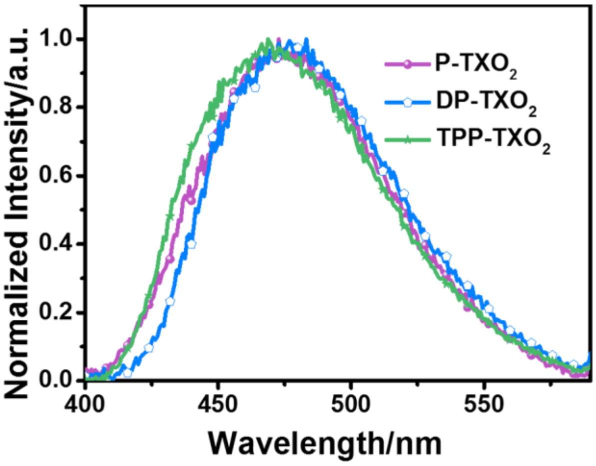

Figure S16. PL spectra of neat thin films of **DP-TXO$_2$**, **P-TXO$_2$** and **TPP-TXO$_2$** (recorded in an integrating sphere λ_{ex} = 330 nm).

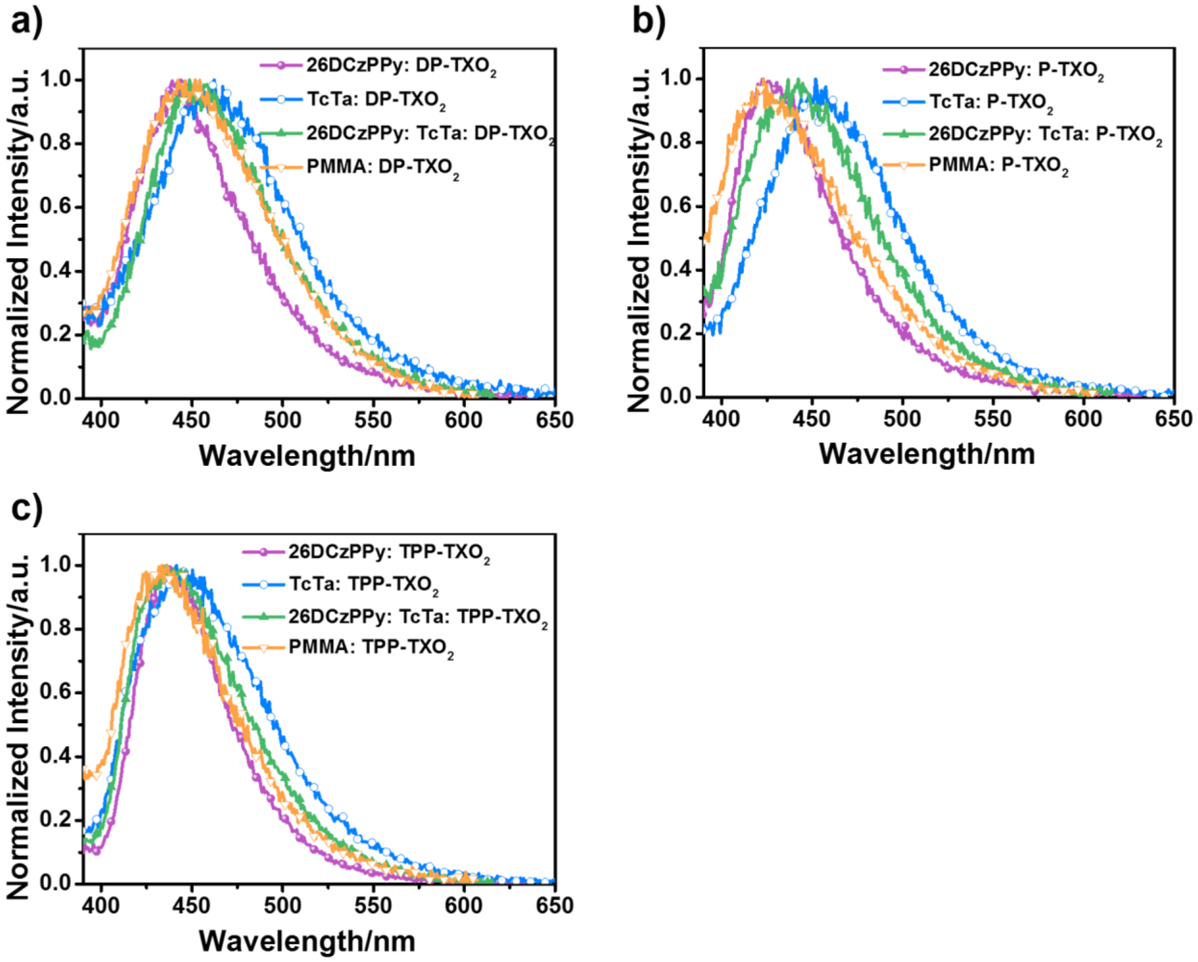

Figure S17. PL spectra of the 12 wt.%-doped thin films in different matrices of a) **DP-TXO$_2$**; b) **P-TXO$_2$**; and c) **TPP-TXO$_2$** (recorded in an integrating sphere, λ_{ex} = 330 nm. For the 26DCzPPy: TcTa film, the doping ration is 1:1 in wt.%).

Table S8. φ_{PL} and λ_{em} values of the 12 wt.%-doped films of the objective compounds in different matrices (λ_{ex} = 330 nm).

Compd.	DP-TXO$_2$		P-TXO$_2$		TPP-TXO$_2$	
	φ_{PL}	λ_{em} [nm]	φ_{PL}	λ_{em}[nm]	φ_{PL}	λ_{em}[nm]
26DCzPPy: **Compd.**	0.41	444	0.45	426	0.52	436
TcTa: **Compd.**	0.15	462	0.19	452	0.28	443
26DCzPPy: TcTa (1:1 in wt.%): **Compd.**	0.27	453	0.27	443	0.39	437
PMMA: **Compd.**	0.48	447	0.48	423	0.47	433

The PL spectra and absolute φ_{PL} values of the 12 wt.%-doped thin films of the objective compounds in different host matrices like PMMA, 26DCzPPy, TcTa, and the mixture of 26DczPPy and TcTa (1:1 in wt.%) are measured on a fluorimeter equipped with in an intergrating sphere, and the corresponding λ_{em} and φ_{PL} data are summarized in Table S8. In comparison with the samples using PMMA or 26DCzPPy as the doping matrix, the films samples using TcTa or 26DczPPy: TcTa as the matrix all show not only red-shifted PL emission band hence much inferior deep-blue chromaticity, but also significantly reduced φ_{PL} values. Since according to the photophysical characterization results of the objective compounds in dilute solution, with increasing solvent polarity, although the contribution from the ^{1}LE and ^{1}CT states may vary, and the PL emission bands will red-shift to some extent, the φ_{PL}s of the ^{1}LE and ^{1}CT states of each of these compounds are quite similar, the red-shifted PL spectra together with lower φ_{PL}s of the films using TcTa or 26DczPPy: TcTa as the doping matrix should be safely ascribed to the formation of exciplex between the objective compounds and the matrix material of TcTa.

Among the film samples of these compounds doped in TcTa matrix, the **DP-TXO$_2$**-based one shows the most red-shifted λ_{em} (462 nm) and the lowest φ_{PL} (0.15), while the **TPP-TXO$_2$**-based sample shows a λ_{em} with the highest energy of 443 nm, together with the highest φ_{PL} of 0.28. Similar trend can be observed in the film samples of these compounds doped in a 26DczPPy: TcTa blending matrix. Because in both dilute solution state and doped-film state in PMMA, **TPP-TXO$_2$** shows a more red-shifted emission band than **DP-TXO$_2$** and **PP-TXO$_2$**, the formation of exciplex should be much more alleviated between **TPP-TXO$_2$** than

DP-TXO$_2$ and **P-TXO$_2$** with TcTa. Taking into consideration that among all the three objective compounds, the exciplex-forming extent in the **DP-TXO$_2$**-based sample is the most severe, and **DP-TXO$_2$** possesses the highest composition of pyrene subunits, and the grafting of a bulky 1,1':3',1"-terphenyl substituent at the pyrene segment is found to allevate the exciplex-formation in the sample, it should be the pyrene moiety that interacts with TcTa to form exciplex.

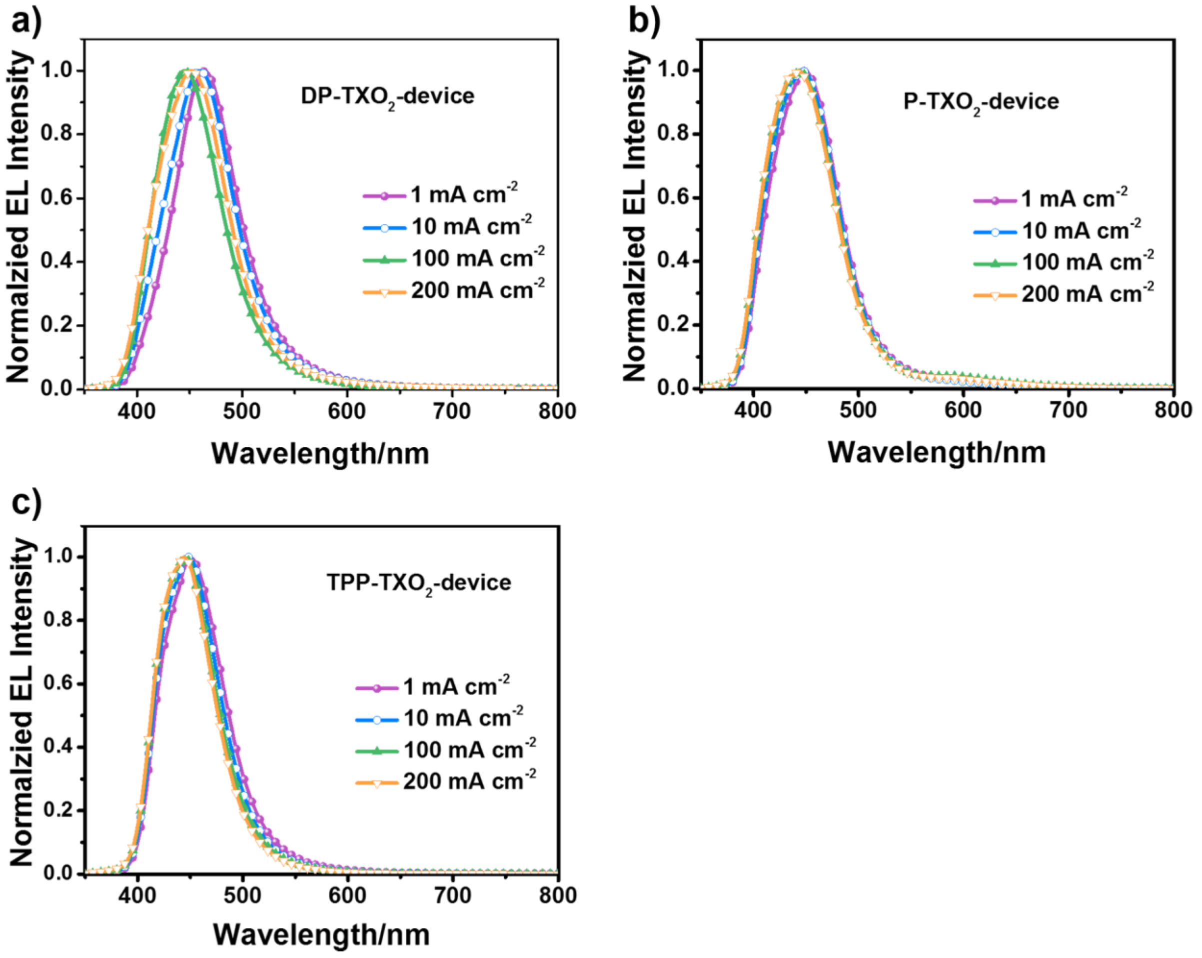

Figure S18. Current density-dependent EL spectra of OLEDs using the objective compounds of: a) **DP-TXO$_2$**; b) **P-TXO$_2$**; and c) **TPP-TXO$_2$** as the doping guest.

With increasing current density, the EL spectrum of the **DP-TXO$_2$**-based device is observed to blue-shift gradually. As the PL spectrum of the first emission layer of TcTa: **DP-**

TXO_2 is more red-shifted than that of the second emission layer of 26DczPPy: **DP-TXO_2**, this variation on the EL spectra of **DP-TXO_2**-based device implies that the exciton recombination region shifts gradually from the TcTa: **DP-TXO_2** layer to the 26DczPPy: **DP-TXO_2** layer gradually under higher driving current density. However, for the **P-TXO_2**- and **TPP-TXO_2**-based OLEDs, under different driving current densities, their EL spectra just vary slightly. This should be attributed to the more fixed exciton recombination region in these two devices, and/or the less significant difference in the PL spectra of **P-TXO_2** and **TPP-TXO_2** in TcTa and 26DczPPy matrices.

Table S9. Calculated exciton utilization efficiencies of OLEDs using the objective molecules as the doping guests.

	DP-TXO_2-based device		**P-TXO_2**-based device		**TPP-TXO_2**-based device	
	EQE_{max} = 4.0%		EQE_{max} = 4.0%		EQE_{max} = 10.5%	
Emission layer	EUE_{max} (η_{out} = 0.2)	EUE_{max} (η_{out} = 0.3)	EUE_{max} (η_{out} = 0.2)	EUE_{max} (η_{out} = 0.3)	EUE_{max} (η_{out} = 0.2)	EUE_{max} (η_{out} = 0.3)
26DCzPPy: **Compd.**	49%	32%	44%	29%	100%	67%
TcTa: **Compd.**	133%	89%	105%	70%	187%	125%
26DCzPPy: TcTa: **Compd.**	74%	49%	74%	49%	138%	92%

To verify the "hot-exciton" mechanism of the objective compounds in OLED applications, the exciton utilization efficiency (EUE) of the three devices is investigated. In OLEDs, the EQE obeys the following equation (12):

$$EQE = \gamma \times \varphi_{PL} \times EUE \times \eta_{out} \qquad (12)^{[7]}$$

where γ is the carrier recombination efficiency, φ_{PL} is the PL efficiency of the emitting layer, EUE is the exciton utilization efficiency in device, and η_{out} is the light out-coupling efficiency. Here, the γ value is assumed to be 100% due to the well-balanced charge carrier injection and transportion in these devices, and the η_{out} values of these devices are assumed to be 0.2–0.3,[7] Considering that in each device, the φ_{PL} values of the two emission layer are different, the EUEs of OLEDs based on **DP-TXO_2**, **P-TXO_2** and **TPP-TXO_2** are calculated to be 32-133%, 29-105%, and 67-187%, in sequence based on the φ_{PL} values of the two emission layers and the interfaces (simulated by the 1:1 mixted TcTa and 26DczPPy). Note that all these calculated EUE values exceed the theoretical limit of 25% branching ratio of singlet exciton yield for conventional fluorescent OLEDs, suggesting the efficient harvesting of triplet excitons in all the OLEDs using the objective compounds as the emitting guest materials.

It should be pointed out that for the **TPP-TXO$_2$**-based device, it shows ultra high EUE values: when η_{out} is assumed to be 0.2, the EUE values of the device is calculated to approach 100% when the highest φ_{PL} value of 0.52 (in 26DCzPPy host material) is employed for the calculation. If lower φ_{PL} values of 0.28 (in TcTa host matrix) and 0.39 (in TcTa:26DCzPPy host matrix) of the emissive layers are used, the EUE values of the device is calculated to be as high as 187% and 138%. Forthermore, even when a higher η_{out} value of 0.3 is used, the EUE values of this device are still calculated to be as high as 67-125%. The ultra-high EUE values of this device together with the rather large $\Delta E_{(\mathrm{S1-T1})}$ of 1.2 eV of **TPP-TXO$_2$** verify the "hot-exciton" mechanism of **TPP-TXO$_2$**.

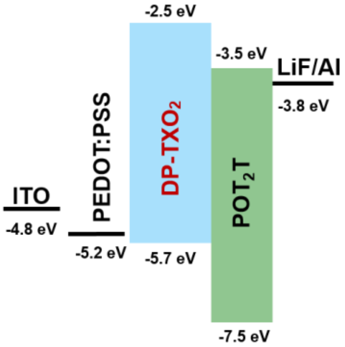

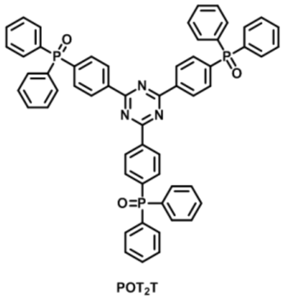

Figure S19. Device configuration and energy-level diagram of the non-doped **DP-TXO$_2$**-based OLED, and the molecular structures of POT$_2$T.

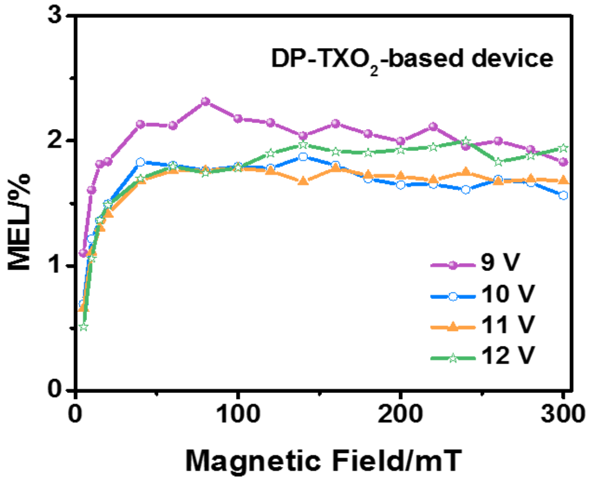

Figure S20. Magnetic field effect of the **DP-TXO$_2$**-based OLED at different bias.

Table S10. Summary of the performances of deep-blue OLEDs with L_{max} of ≥ 4000 cd m^{-2}, EQE_{max} of >5.0 %, and CIE 1931 coordinates (x, y) of CIE $0.04 \leq y \leq 0.1$.

Compound	L_{max} [cd m^{-2}]	EQE_{max}	EQE @1000cd/m^2	CIE 1931 coordinates (x, y)	Ref.
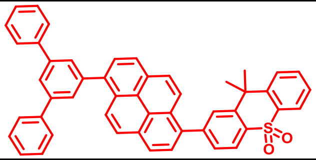	**10480**	**10.5%**	**4.6%**	**(0.152, 0.065)**	**This work**
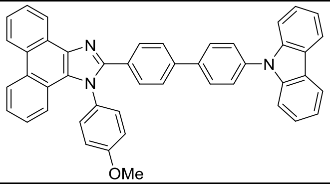	6450	5.97%	~4.8%	(0.16, 0.08)	8
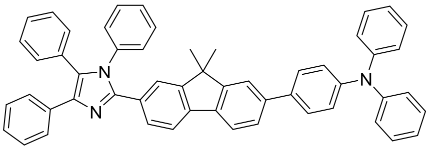	7490	5.74%	~4%	(0.152, 0.054)	9
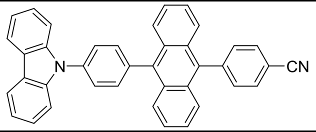	8044	9.23%	7.10%	(0.14, 0.10)	10
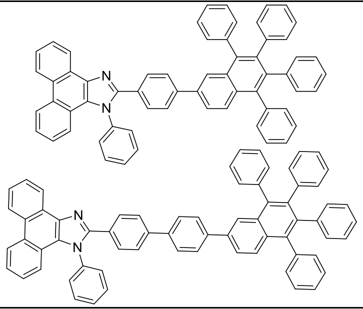	7000 5000	5.2% 5.75%	5.08% 5.70%	(0.152, 0.080) (0.153, 0.082)	11
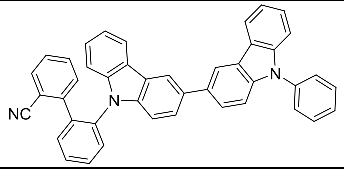	~14300	11.9%	9%	(0.16, 0.10)	12
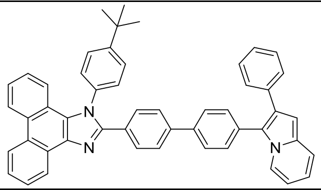	14350	6.01%	5.33%	(0.151, 0.076)	13
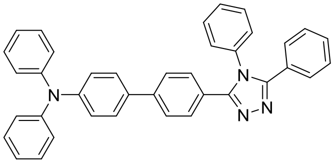	4970	5.92%	~4.3%	(0.155, 0.047)	14
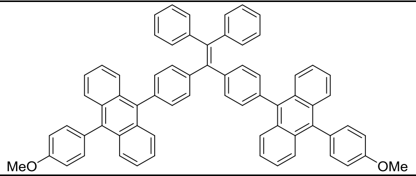	6527	8.0%	3.9%	(0.15, 0.09)	15

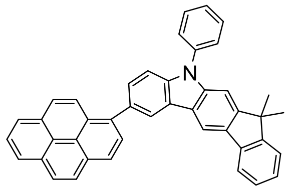	~10000	6.08%	5.35%	(0.15, 0.08)	16
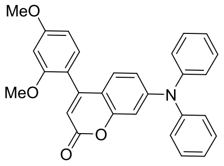 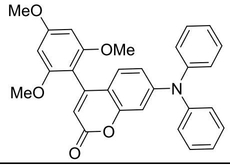	7340 7800	5.2% 5.1%	4.3% 3.2%	(0.145, 0.093) (0.148, 0.084)	17
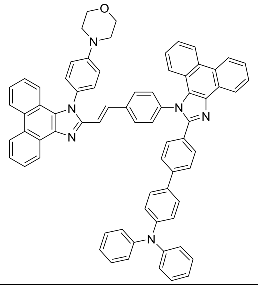	12680	6.1%	~2%	(0.16, 0.08)	18
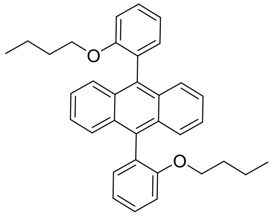	~4300	10.27%	8.70%	(0.15, 0.05)	19
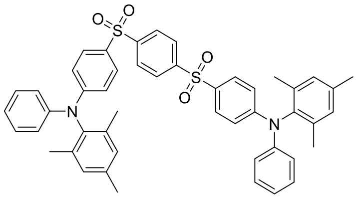	10388	8.9%	~2.8%	(0.16, 0.08)	20
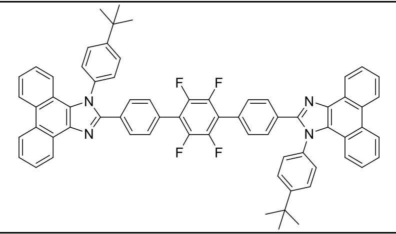	~4000	6.94%	4.97%	(0.15, 0.09)	21
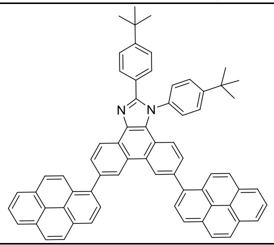	~4500	5.78%	~5.6%	(0.153, 0.099)	22

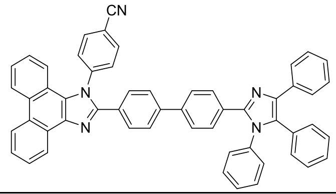	9718	5.80%	~4.8%	(0.15, 0.07)	23
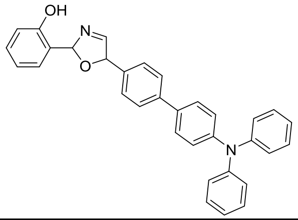	9054	7.1%	4.8%	(0.15, 0.08)	24
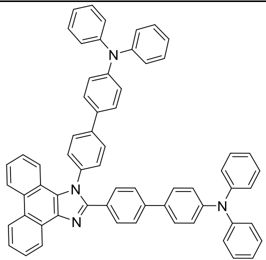	14850	7.20%	~6%	(0.150, 0.063)	25
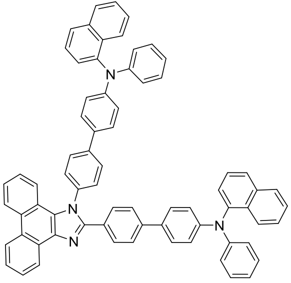	18105	6.33%	~5.8%	(0.151, 0.066)	
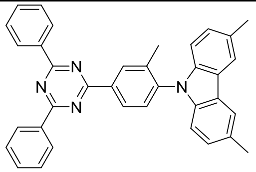	~4000	19.2%	~7%	(0.148, 0.098)	26
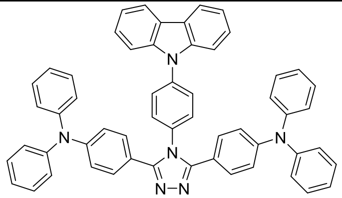	7323	6.8%	~5%	(0.158, 0.043)	27
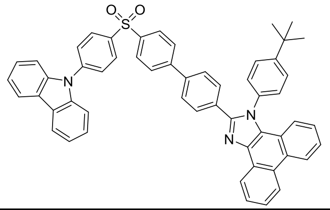	5225	5.43%	~3.5%	(0.151, 0.072)	28
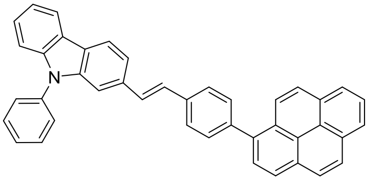	~20000	9.1%	6%	(0.15, 0.09)	29

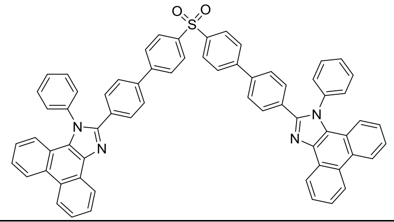	15598	6.8%	5.64%	(0.152, 0.077)	30
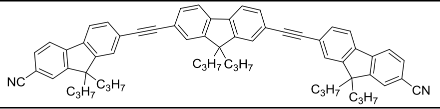	6828	~8%	3.7%	(0.159, 0.050)	31
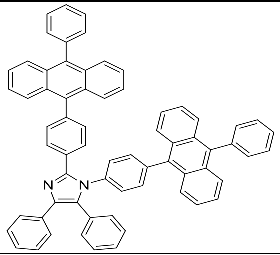	9505 13408	5.1% 6.5%	3.6% 6.5%	(0.15, 0.05) (0.15, 0.08)	32
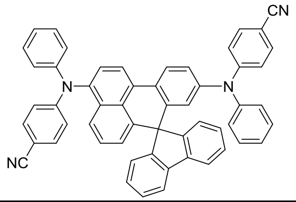	~5000 >6000	10.7% 12.6%	7.5% 9.5%	(0.15, 0.08) (0.15, 0.10)	33
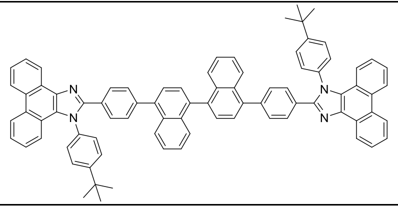	~5000	5.95%	-	(0.15, 0.09)	34
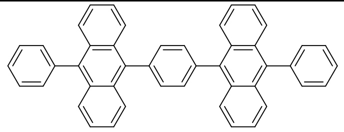	~4500	8.9%	3.7%	(0.16, 0.05)	35
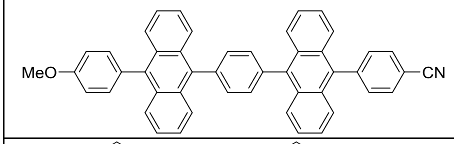	~4000	12%	4.2%	(0.15, 0.06)	
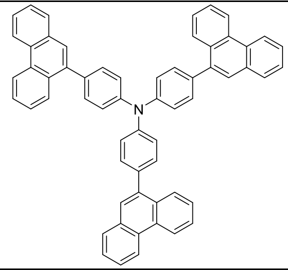	11970	7.23%	-	(0.157, 0.073)	36
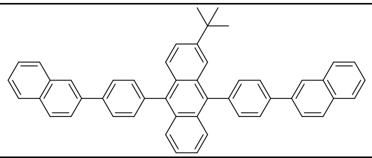	6940	5.17%	~1.8%	(0.149, 0.086)	37
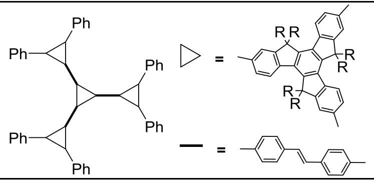	17000	6.6%	6.2%	(0.155, 0.086)	38

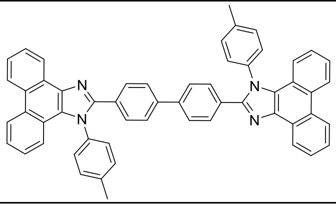	17300	5.43%	-	(0.15, 0.09)	39

II. Experimental

1) General information. All the reagents and solvents used for the synthesis were commercially available and used as received. All the solvents used for the measurements were of analytical grades and freshly distilled prior to use. The ^{1}H NMR and ^{13}C NMR spectra were recorded on a Bruker Advanced II (400 MHz) spectrometer with $CDCl_3$ as the solvent and tetramethylsilane (TMS) as an internal reference. High resolution MS spectra were obtained from a Q-TOF Premier ESI mass spectrometer (Micromass, Manchester, UK). The crystallographic data for **P-TXO$_2$** and **DP-TXO$_2$** reported here have been deposited in the Cambridge Structural Database (CCDC 1894319, 1894318). Single crystal X-ray diffraction data of **DP-TXO$_2$** was obtained on a New Gemini E X-ray single crystal diffractometer equipped with a graphite monochromator CuKα (λ = 1.54184 Å) radiation. The crystal was kept at 298.2 K during data collection. Using Olex2,[40] the structure was solved with the olex2.solve[41] structure solution program using charge flipping and refined with the ShelXL[42] refinement package using Least Squares minimisation. Single crystal X-ray diffraction data of **P-TXO$_2$** was obtained on a Xcalibur E X-ray single crystal diffractometer equipped with a graphite monochromator Mo-Kα (λ = 0.71073 Å) radiation. The crystal was kept at 293.2 K during data collection. Using Olex2,[40] the structure was solved with the Superflip[43] structure solution program using charge flipping and refined with the ShelXL[44] refinement package using Least Squares minimisation. Differential scanning calorimetry (DSC) data was performed using a DSC 200PC (rate = 10 ℃ min^{-1}, range = 20 to 350 ^{o}C). Thermogravimetric analysis (TGA) was carried out using DTG-60(H) at a heating rate of 10 ℃ min^{-1} under N_2 atmosphere. Fluorescence spectra were collected on a Horiba Jobin Yvon-Edison Fluoromax-4 fluorescence spectrometer. UV-Vis absorption spectra were obtained on a UV 2600 spectrophotometer. The concentration of solution samples for PL measurements was 2×10^{-6} mol L^{-1}. Relative PL quantum yields (φ_{PL}) of the solution samples were measured at room temperature in 2×10^{-6} mol L^{-1} solutions, using quinoline sulfate as the reference ($\varphi_{PL} = 0.55$).[45] The doped films of compounds were spin-coated from their corresponding 1,2-dichloroethane solutions with a concentration of 10 mg mL^{-1} at a speed of 1500 rpm on quartz substrates for 30 s. Cyclic voltammetry measurements were performed in anhydrous dichloromethane solutions(5×10^{4} mol L^{-1}) of the compounds using 0.10 mol L^{-1} Bu_4NClO_4 as the supporting electrolyte under a N_2 atmosphere on a LK 2010 electrochemical work station at room temperature, and the three-electrode cell comprised a Pt working electrode, a Pt wire counter electrode, and a $Ag/AgNO_3$ (0.1 M in acetonitrile) reference electrode. A ferrocene/ferrocenium redox couple (Fc/Fc^+) was employed as the external standard. The PL lifetimes were measured by time-correlated single-photon counting (TCSPC) system on a HORIBA Jobin Yvon Fluorolog-3 fluorescence spectrometer. The absolute φ_{PL}s of the film samples were determined on a HORIBA Jobin Yvon Fluorolog-3 fluorescence spectrometer equipped with an integrating sphere (IS80 from Labsphere) and a digital photometer (S370 from UDT) under ambient conditions. PL spectra at 77~295 K were recorded on a Horiba Jobin Yvon Fluorolog-3 fluorescence spectrophotometer.

2) Quantum chemical calculations. Theoretical simulations were performed using the Gaussian 09 software packages.[46] The geometries were optimized at the B3LYP/6-311g* level.[47] And the electronic properties of the emitters were calculated by TD-DFT[48] procedure at the TD-B3LYP/6-311g* level. The geometries and FMO distributions were visualized using Gaussview. In all the calculations, the solvent effects were simulated using the SCRF/PCM model.[49] The solvent used for our calculations was *n*-hexane.

3) **OLED fabrication and measurements**. The charge carrier injecting and transporting materials and host materials for fabrication of OLEDs were obtained commercially and used as received without further purification. Indium-tin-oxide (ITO) coated glass with a sheet resistance of 15 Ω sq^{-1} was used as the anode substrate. Prior to film deposition, pre-patterned ITO substrates were cleaned with detergent, rinsed in de-ionized water, dried in an oven, and

finally treated with oxygen plasma for 10 minutes at a pressure of 10 Pa to enhance the surface work function of ITO anode (from 4.7 to 5.1 eV). All the organic layers were deposited with a rate of 0.1 nm s^{-1} under high vacuum ($\leq 3 \times 10^{-5}$ Pa). The light-emitting layers were prepared by co-evaporation of the guest and host materials from two individual sources, and the doping concentrations were modulated by controlling the evaporation rate of the dopant and host. LiF and Al were deposited in another vacuum chamber ($\leq 8.0 \times 10^{-5}$ Pa) with the rates of 0.01 and 1 nm s^{-1}, respectively, without being exposed to the atmosphere. The thickness of these deposited layers and the evaporation rate of different materials were monitored in vacuum with quartz crystal monitors. A shadow mask was used to define the cathode so that the emission area of the devices is 10 mm^2. Current density-voltage-luminance (J-V-L) characteristics of the devices were measured by using a programmable Keithley source measurement unit (Keithley 2400 and Keithley 2000) with a silicon photodiode. Electroluminescence (EL) spectra were obtained with a calibrated Hitachi F-7000 fluorescence spectrophotometer.

Synthesis and structural characterization.

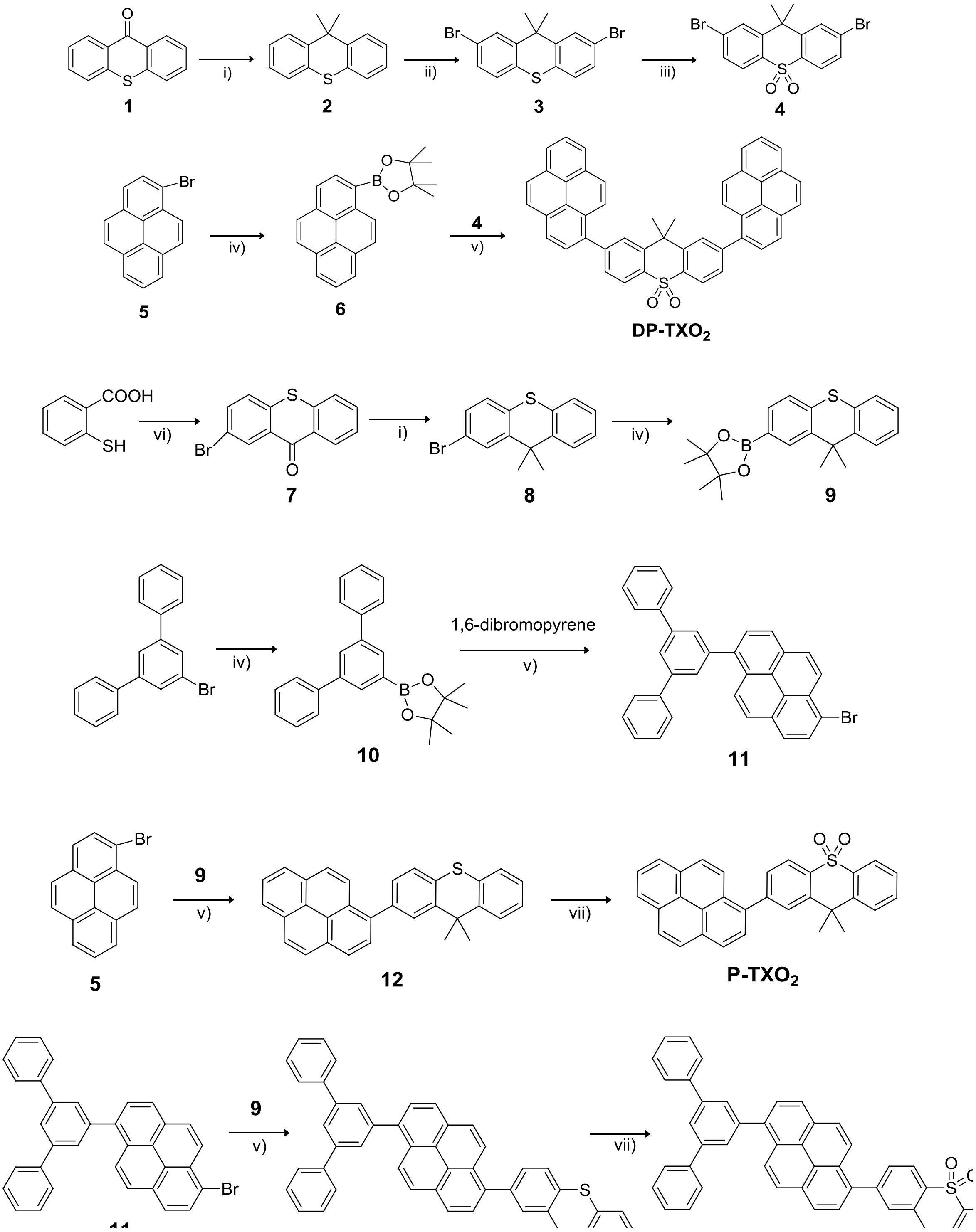

Reaction conditions: i) Al(Me)$_3$, Tol; ii) Br$_2$, CH$_2$Cl$_2$; iii) H$_2$O$_2$, AcOH; iv) B$_2$pin$_2$, KOAc, Pd(dppf)Cl$_2$, 1,4-dioxane; v) Pd(PPh$_3$)$_4$, Na$_2$CO$_3$, Tol, EtOH; vi) bromobenzene, 98% H$_2$SO$_4$; vii) 3-chloroperbenzoic acid, CH$_2$Cl$_2$.

Scheme S1. Synthetic routes to the objective compounds.

Synthesis of 9,9-dimethyl-9*H*-thioxanthene (2)[50]

1 (2 g, 9.4 mmol) and dry toluene (30 mL) were added to a 100 mL three-necked flask, then a solution of trimethylaluminum (33.6 mmol) in *n*-hexane (21 mL) was added dropwise via a dropping funnel at 0 °C under argon, follwed by continuous stiring for 17 h at room temperature. Then the reaction mixture was poured into a mixture of concentrated hydrochloric acid (8 mL) and iced water (20 mL), then extracted with CH_2Cl_2 (40 mL × 3). The combined organic phase was dried over anhydrous Na_2SO_4. After removing the solvent, the residue was purified by column chromatography on silica gel employing petroleum ether (PE) as an eluent, and an oily liquid was obtained in a yield of 98%. ^{1}H NMR (400 Hz, $CDCl_3$) $\delta = 7.52$ (dd, $J_1 = 8.0$ Hz, $J_2 = 1.2$ Hz, 2 H; ArH), 7.43 (dd, $J_1 = 7.6$ Hz, $J_2 = 1.6$ Hz, 2 H; ArH), 7.26 (td, $J_1 = 7.6$ Hz, $J_2 = 1.2$ Hz, 2 H; ArH), 7.18 (t, $J_1 = 7.6$ Hz, $J_2 = 1.2$ Hz, 2 H; ArH), 1.68 ppm (s, 6 H; CH_3).

Synthesis of 2,7-dibromo-9,9-dimethyl-9*H*-thioxanthene (3)[50]

Bromine (0.3 mL, 5.85 mmol) was slowly added to a solution of **2** (600 mg, 2.65 mmol) in CH_2Cl_2 (15 mL) at 0 °C, then the reaction mixture was allowed to warm to room temperature followed by continuous stiring for 15 h. Then the reaction mixture was poured into 10 mL aqueous sodium thiosulfate (20 wt.%), and extracted with CH_2Cl_2 (20 mL × 3). The combined organic layers were washed with water (30 mL × 3) and brine (30 mL × 2), and then dried over anhydrous Na_2SO_4. After the removement of solvent, pure product as a light yellow solid was obtained with a yield of 69%. ^{1}H NMR (400 Hz, $CDCl_3$) $\delta = 7.62$ (d, $J = 2.0$ Hz, 2 H; ArH), 7.33 (dd, $J_1 = 8.0$ Hz, $J_2 = 2.0$ Hz, 2 H; ArH), 7.28 (d, $J = 8.4$ Hz, 2 H; ArH), 1.64 ppm (s, 6 H; CH_3).

Synthesis of 2,7-dibromo-9,9-dimethyl-9*H*-thioxanthene-10,10-dioxide (4)[50]

3 (500 mg, 1.20 mmol) was dissolved in acetic acid (25 mL) and stirred at 80 °C for 0.5 h, then H_2O_2 (7 mL, 30 wt.% in H_2O) was added dropwise via a dropping funnel. After the addition, the mixture was refluxed for 2 h. After cooled down to room temperature, the precipitation was collected by filtration, and washed with water to afford the product. After being dried at 70 °C overnight, the product was obtained as a white solid, and the yield is 98%. ^{1}H NMR (400 Hz, $CDCl_3$,) δ = 8.15 (d, J = 2.0 Hz, 2 H; ArH), 8.05 (d, J = 8.4 Hz, 2 H; ArH), 7.86 (dd, J_1 = 8.4 Hz, J_2 = 2.0 Hz, 2H), 1.96 ppm (s, 6 H; CH_3).

Synthesis of 4,4,5,5-tetramethyl-2-(pyren-1-yl)-1,3,2-dioxaborolane (6)[51]

1-bromopyrene (200 mg, 0.71 mmol), Pd(dppf)Cl_2 (26.3 mg, 0.036 mmol), bis(pinacolato)diborane (360 mg, 1.42 mmol) and KOAc (208 mg, 2.13 mmol) were dissolved in 1,4-dioxane (10 mL) under argon. The reaction mixture was degassed with argon and stirred at 90 °C for 16 h. After the completion of the reaction, the mixture was poured into water. After extraction with CH_2Cl_2 (20 mL × 3), the resultant organic phase was washed with brine, and dried over anhydrous Na_2SO_4. After removing the solvent, the residue was purified using column chromatography on silica gel employing CH_2Cl_2/PE (1/5) as an eluent to afford a yellow powdery solid with a yield of 73%. ^{1}H NMR (400 Hz, $CDCl_3$) δ = 8.98 (d, J = 9.2 Hz, 1 H; ArH), 8.44 (d, J = 8.0 Hz, 1 H; ArH), 8.09 (d, J = 7.6 Hz, 1 H; ArH), 8.05 (d, J = 8.0 Hz, 1 H; ArH), 8.04 (t, J = 9.2 Hz, 2 H; ArH), 7.96 (apparent-q, J = 8.8 Hz, 2 H; ArH), 7.87 (t, J = 7.6 Hz, 1 H; ArH), 1.37 ppm (s, 12 H; CH_3).

Synthesis of 9,9-dimethyl-2,7-di(pyren-1-yl)-9*H*-thioxanthene-10,10-dioxide (DP-TXO$_2$)

To a solution of **6** (100 mg, 0.31 mmol) and **4** (58 mg, 0.14 mmol) in mixed solvents of toluene (10 mL) and ethanol (2 mL) were added $Pd(PPh_3)_4$ (19 mg, 0.017 mmol) and aqueous Na_2CO_3 (0.69 mL, 2 mol L^{-1}) under argon. The reaction mixture was stirred at 100 °C for 38 h under argon. After the completion of the reaction, the reaction mixture was cooled down, then poured into 50 mL water and extracted with CH_2Cl_2 (20 mL × 3). The resultant organic phase was washed with brine, and dried over anhydrous Na_2SO_4. After removing the solvent, the residue was purified using column chromatography on silica gel employing CH_2Cl_2/PE (1/1) as an eluent to give a pale yellow solid with a yield of 80%. ^{1}H NMR (400 Hz, $CDCl_3$) δ = 8.47 (d, J = 8.0 Hz, 2 H; ArH), 8.27 (d, J = 8.0 Hz, 2 H; ArH), 8.24 (dd, J_1 = 7.6 Hz, J_2 = 0.8 Hz, 2 H; ArH), 8.21 (dd, J_1 = 7.6 Hz, J_2 = 0.8 Hz, 2 H; ArH), 8.14 (apparent-q, J = 9.2 Hz, 4 H; ArH), 8.09 (s, 4 H; ArH), 8.05 (t, J = 8.0 Hz, 4 H; ArH), 7.99 (d, J = 8.0 Hz, 2 H; ArH), 7.84 (dd, J_1 = 8.0 Hz, J_2 = 1.2 Hz, 2 H; ArH), 2.05 ppm (s, 6 H; CH_3). ^{13}C NMR (100 Hz, $CDCl_3$) δ = 146.2, 146.1, 135.8, 135.7, 131.5, 131.3, 130.9, 129.7, 128.5, 128.3, 128.2, 128.1, 127.3, 126.3, 125.6, 125.3, 125.0, 124.8, 124.5, 124.4, 39.7, 31.2. HRMS (ESI) *m/z*: $[M + H]^+$ calcd. for $C_{47}H_{31}O_2S^+$, 659.2039; found, 659.2043.

Synthesis of 2-bromo-9*H*-thioxanthen-9-one (7)[52]

2-mercaptobenzoic acid (400 mg, 2.6 mmol), concentrated sulfuric acid (98%, 4 mL) and bromobenzene (0.56 mL, 5.36 mmol) were added to a 100 mL three-necked flask. The mixture was stirred for 24 h at room temperature, then stirred at 100 °C for 1 h. After cooling to room temperature, water (30 mL) was added, and the mixture was extracted with CH_2Cl_2 (30 mL × 2). The combined organic layers were washed with water (30 mL × 3) and dried over anhydrous Na_2SO_4. After removing the solvent, the residue was purified using column chromatography on silica gel employing toluene as an eluent to afford a primrose yellow solid with a yield of 63%. ^{1}H NMR (400 Hz, $CDCl_3$) δ = 8.75 (d, J = 2.4 Hz, 1 H; ArH), 8.61 (dd, J_1 = 8.0 Hz, J_2 = 1.2 Hz, 1 H; ArH), 7.72 (dd, J_1 = 8.4 Hz, J_2 = 2.4 Hz, 1 H; ArH), 7.65 (td, J_1 = 8.0 Hz, J_2 = 1.6 Hz, 1 H; ArH), 7.58 (dd, J_1 = 8.0 Hz, J_2 = 1.2 Hz, 1 H; ArH), 7.51 (td, J_1 = 8.4 Hz, J_2 = 1.2 Hz, 1 H; ArH) 7.47 ppm (d, J = 8.4 Hz, 1 H; ArH).

Synthesis of 2-bromo-9,9-dimethyl-9*H*-thioxanthene (8)

Intermediate **8** was prepared as a colourless oily liquid with a yield of 98% using a similar procedure for the synthesis of **2**, but with **7** rather than **1** as the reactant. ^{1}H NMR (400 Hz, $CDCl_3$) δ = 7.62 (d, J = 1.2 Hz, 1 H; ArH), 7.50 (dd, J_1 = 8.0 Hz, J_2 = 1.2 Hz, 1 H; ArH), 7.42

(dd, J_1 = 7.6 Hz, J_2 = 1.6 Hz, 1 H; ArH), 7.30-7.29 (m, 2 H; ArH), 7.26 (td, J_1 = 8.0 Hz, J_2 = 1.6 Hz, 1 H; ArH), 7.19 (td, J_1 = 7.6 Hz, J_2 = 1.2 Hz, 1 H; ArH), 1.65 ppm (s, 6 H; CH_3).

Synthesis of 2-(9,9-dimethyl-9*H*-thioxanthen-2-yl)-4,4,5,5-tetramethyl-1,3,2-dioxaborolane (9)

Intermediate **9** was prepared as a white solid with a yield of 47% using a similar procedure for the synthesis of **6**, but with **8** rather than 1-bromopyrene as the reactant. ^{1}H NMR (400 Hz, $CDCl_3$) δ = 7.93 (d, J = 0.8 Hz, 1 H; ArH), 7.62 (dd, J_1 = 7.6 Hz, J_2 = 1.2 Hz, 1 H; ArH), 7.53 (dd, J_1 = 8.0 Hz, J_2 = 1.2 Hz, 1 H; ArH), 7.43 (d, J = 7.6 Hz, 1 H; ArH), 7.42 (dd, J_1 = 7.6 Hz, J_2 = 1.2 Hz, 1 H; ArH), 7.25 (td, J_1= 8.0 Hz, J_2= 1.6 Hz, 1 H; ArH), 7.18 (td, J_1 = 7.6 Hz, J_2 = 1.2 Hz, 1 H; ArH), 1.70 (s, 6 H; CH_3), 1.34 ppm (s, 12 H; CH_3).

Synthesis of 2-([1,1':3',1''-terphenyl]-5'-yl)-4,4,5,5-tetramethyl-1,3,2-Dioxaborolane (10)[53]

Intermediate **10** was prepared as a white solid with a yield of 70% using a similar procedure for the synthesis of **6**, but with 5'-bromo-1,1':3',1"-terphenyl rather than 1-bromopyrene as the reactant. ^{1}H NMR (400 Hz, $CDCl_3$) δ = 8.03 (d, J = 2.0 Hz, 2 H; ArH), 7.90 (t, J = 2.0 Hz, 1 H; ArH), 7.68 (dd, J_1 = 8.4 Hz, J_2 = 1.2 Hz, 4 H; ArH), 7.44 (td, J_1 = 6.4 Hz, J_2 = 1.6 Hz, 4 H; ArH), 7.35 (tt, J_1 = 7.2 Hz, J_2 = 1.2 Hz, 2 H; ArH), 1.38 ppm (s, 12 H; CH_3).

Synthesis of 1-([1,1':3',1''-terphenyl]-5'-yl)-6-bromopyrene (11)

To a solution of 1,6-dibromopyrene (4 g, 11.07 mmol) and **10** (3.28 g, 9.23 mmol) in mixed solvent of toluene (125 mL) and ethanol (25 mL) were added $Pd(PPh_3)_4$ (360 mg, 0.26 mmol) and aqueous Na_2CO_3 (12 mL, 2 mol L^{-1}) under argon. The reaction mixture was stirred at 90 ^oC for 8 h under argon, then cooled down and poured into 50 mL water. After extraction with CH_2Cl_2 (20 mL × 3), the resultant organic phase was washed with brine, and dried over anhydrous Na_2SO_4. After removing the solvent, the residue was purified using column chromatography on silica gel employing CH_2Cl_2 /PE (9/1) as an eluent to give a white solid with a yield of 42%. ^{1}H NMR (400 Hz, $CDCl_3$) δ = 8.44 (d, J = 9.2 Hz, 1 H; ArH), 8.29 (d, J

= 9.2 Hz, 1 H; ArH), 8.26 (d, J = 7.6 Hz, 1 H; ArH), 8.21 (d, J = 8.0 Hz, 1 H; ArH), 8.17 (d, J = 9.2 Hz, 1 H; ArH), 8.09 (d, J = 8.0 Hz, 1 H; ArH), 7.95 (d, J = 7.6 Hz, 2 H; ArH), 7.94 (s, 1 H; ArH), 7.82 (d, J = 1.2 Hz, 2 H; ArH), 7.74 (d, J = 7.6 Hz, 4 H; ArH), 7.47 (t, J = 7.6 Hz, 4 H; ArH), 7.38 ppm (t, J = 7.2 Hz, 2 H; ArH).

Synthesis of 9,9-dimethyl-2-(pyren-1-yl)-9*H*-thioxanthene (12)

Intermediate **12** was prepared as a pale yellow solid with a yield of 49% using a similar procedure for the synthesis of **11**, but with 1-bromopyrene and **9** rather than 1,6-dibromopyrene and **10** as the reactant. ^{1}H NMR (400 Hz, $CDCl_3$) δ = 8.22 (d, J = 8.0 Hz, 1 H; ArH), 8.19 (d, J = 7.6 Hz, 1 H; ArH), 8.16 (d, J = 7.2 Hz, 1 H; ArH), 8.14 (dd, J_1 = 9.2 Hz, J_2 = 1.2 Hz, 1 H; ArH), 8.10 (s, 2 H; ArH), 8.02 (d, J = 9.6 Hz, 1 H; ArH), 8.01 (t, J = 8.0 Hz, 1 H; ArH), 7.98 (dd, J_1 = 7.6 Hz, J_2 = 1.2 Hz, 1 H; ArH), 7.79 (t, J = 1.6 Hz, 1 H; ArH), 7.63 (dd, J_1 = 8.0 Hz, J_2 = 1.2 Hz, 1 H; ArH), 7.58 (d, J = 7.6 Hz, 1 H; ArH), 7.52 (m, 1 H; ArH), 7.47 (dd, J_1 = 8.0 Hz, J_2 = 1.6 Hz, 1 H; ArH), 7.31 (td, J_1 = 7.6 Hz, J_2 = 1.2 Hz, 1 H; ArH), 7.24 (td, J_1 = 8.8 Hz, J_2 = 1.2 Hz, 1 H; ArH), 1.76 ppm (s, 6 H; CH_3).

Synthesis of 2-(6-([1,1':3',1''-terphenyl]-5'-yl)pyren-1-yl)-9,9-dimethyl-9*H*-thioxanthene (13)

Intermediate **13** was prepared as a pale yellow solid with a yield of 52% using a similar procedure for the synthesis of **12**, but with **11** rather than 1-bromopyrene as the reactant. ^{1}H NMR (400 Hz, $CDCl_3$) δ = 8.31 (d, J = 9.2 Hz, 1 H; ArH), 8.22 (t, J = 8.4 Hz, 2 H; ArH), 8.17 (d, J = 9.2 Hz, 1 H; ArH), 8.09 (d, J = 8.0 Hz, 1 H; ArH), 8.06 (d, J = 7.2 Hz, 1 H; ArH), 8.04 (d, J = 7.2 Hz, 1 H; ArH), 7.98 (d, J = 8.0 Hz, 1 H; ArH), 7.94 (t, J = 1.6 Hz, 1 H; ArH), 7.86 (d, J = 2.0 Hz,2 H; ArH), 7.81 (s, 1 H; ArH), 7.77 (d, J = 8.0 Hz, 4 H; ArH), 7.63 (d, J = 8.0 Hz, 1 H; ArH), 7.58 (dd, J_1 = 8.0 Hz, J_2 = 1.2 Hz, 1 H; ArH), 7.53 (d, J = 7.2 Hz, 2 H; ArH),7.52 (dd, J_1= 8.0 Hz, J_2 = 1.6 Hz, 1 H; ArH), 7.49 (d, J = 8.0 Hz, 4 H; ArH), 7.39 (tt, J_1 = 7.6 Hz, J_2 = 1.2 Hz, 2 H; ArH), 7.31 (td, J_1 = 7.6 Hz, J_2 = 1.6 Hz, 1 H; ArH), 7.24 (td, J_1 = 7.6 Hz, J_2 = 1.2 Hz, 2 H; ArH), 1.76 ppm (s, 6 H; CH_3).

Synthesis of 9,9-dimethyl-2-(pyren-1-yl)-9*H*-thioxanthene 10,10-dioxide (P-TXO$_2$)

To a solution of **12** (100 mg, 0.23 mmol) in CH_2Cl_2 (10 mL) was added 3-chloroperbenzoic acid (162 mg, 0.94 mmol). The mixture was stirred for 1 h at room temperature, then the pH value of the mixture was adjusted to 7.0 with aqueous Na_2CO_3(2 mol L^{-1}). The mixture was extracted with CH_2Cl_2 (20 mL × 3), and the resultant organic phase was washed with brine, and dried over anhydrous Na_2SO_4. After removing the solvent, the residue was purified using column chromatography on silica gel employing CH_2Cl_2/PE (1/1) as an eluent to afford a yellow solid with a yield of 20%. ^{1}H NMR (400 Hz, $CDCl_3$) δ = 8.39 (d, J = 8.0 Hz, 1 H; ArH), 8.28 (dd, J_1 = 7.6 Hz, J_2 = 1.6 Hz, 1 H; ArH), 8.25 (td, J_1 = 7.6 Hz, J_2 = 0.8 Hz, 2 H; ArH), 8.20 (dd , J_1 = 7.6 Hz, J_2 = 0.8 Hz, 1 H; ArH), 8.13 (apparent-q, J = 9.2 Hz, 2 H; ArH), 8.08-8.03 (m, 3 H; ArH), 8.00 (d, J = 1.6 Hz,1 H; ArH), 7.96 (d, J = 8.0 Hz, 1 H; ArH), 7.79 (dd, J_1 = 8.0 Hz, J_2 = 0.8 Hz, 1 H; ArH), 7.78 (dd, J_1 = 8.0 Hz, J_2 = 1.6 Hz, 1 H; ArH), 7.64 (td, J_1= 8.0 Hz, J_2 = 1.6 Hz, 1 H; ArH), 7.56 (td, J_1 = 7.6 Hz, J_2 = 1.2 Hz, 1 H; ArH), 1.97 ppm (s, 6 H; CH_3). ^{13}C NMR (100 Hz, $CDCl_3$) δ = 146.1, 145.9, 136.9, 135.9, 135.5, 133.0, 131.5, 130.8, 129.6, 128.3, 128.1, 127.6, 127.3, 126.3, 125.8, 125.6, 125.3, 125.0, 124.8, 124.7, 124.5, 124.4, 39.6, 31.2. HRMS (ESI) *m/z*: $[M + H]^+$ calcd. for $C_{31}H_{23}O_2S^+$, 459.1413; found, 459.1414.

Synthesis of 2-(6-([1,1':3',1''-terphenyl]-5'-yl)pyren-1-yl)-9,9-dimethyl-9*H*-thioxanthene-10,10-dioxide (TPP-TXO$_2$)

Compound **TPP-TXO$_2$** was prepared as a white solid with a yield of 26% using a similar procedure for the synthesis of **P-TXO$_2$**, but with **13** rather than **12** as the reactant. ^{1}H NMR (400 Hz, $CDCl_3$) δ = 8.40 (d, J = 8.0 Hz, 1 H; ArH), 8.36 (d, J = 9.2 Hz, 1 H; ArH), 8.28 (dd, J_1 = 7.6 Hz, J_2 = 1.6 Hz, 1 H; ArH), 8.27 (d, J = 8.0 Hz, 1 H; ArH), 8.24 (d, J = 8.0 Hz, 1 H; ArH), 8.13 (d, J = 7.6 Hz, 1 H; ArH), 8.10-8.07 (m, 3 H; ArH), 8.02 (d, J = 1.2 Hz, 1 H; ArH), 7.97 (d, J = 8.0 Hz, 1 H; ArH), 7.96 (t, J = 1.6 Hz, 1 H; ArH), 7.87 (d, J = 1.6 Hz, 2 H; ArH), 7.80 (dd, J_1 = 8.0 Hz, J_2 = 1.6 Hz, 2 H; ArH), 7.77 (dd , J_1 = 8.4 Hz, J_2 = 1.6 Hz, 4 H; ArH), 7.65 (td, J_1 = 7.6 Hz, J_2 = 1.6 Hz,1 H; ArH), 7.57 (td, J_1 = 7.6 Hz, J_2 = 0.8 Hz, 1 H; ArH), 7.50 (t , J = 8.0 Hz, 4 H; ArH), 7.41 (tt, J_1 = 7.2 Hz, J_2 = 2.0 Hz, 2 H; ArH), 1.98 ppm (s, 6 H; CH_3). ^{13} C NMR (100 Hz, $CDCl_3$) δ = 146.2, 146.1, 145.9, 142.1, 142.0, 141.0, 138.1, 136.9, 136.0, 135.5, 133.0, 131.1, 130.4, 129.7, 128.9, 128.8, 128.4, 128.3, 128.1, 127.7, 127.6, 127.5, 127.4, 125.9, 125.8, 125.2, 125.1, 125.0, 124.7, 124.5, 124.4, 124.3, 39.5, 31.0. HRMS (ESI) *m*/*z*: $[M + H]^+$ calcd. for $C_{49}H_{35}O_2S^+$, 687.2352; found, 687.2296.

III. References

[1] K. A. Zachariasse, S. I. Druzhinin, W. Bosch and R. Machinek, *J. Am. Chem. Soc.*, 2004, **126**, 1705.

[2] S. Mukherjee, A. Chattopadhyay, A. Samanta and T. Soujanya, *J. Phys. Chem.*, 1994, **98**, 2809.

[3] Y. Niko, S. Kawauchi and G.-i. Konishi, *Chem. Eur. J.*, 2013, **19**, 9760.

[4] a) J. Liu, Z. Li, T. Hu, X. Wei, R. Wang, X. Hu, Y. Liu, Y. Yi, Y. Yamada-Takamura, Y. Wang and P. Wang, *Adv. Opt. Mater.*, 2019, **7**, 1801190; b) N. A. Drigo, L. G. Kudriashova, S. Weissenseel, A. Sperlich, A. J. Huckaba, M. K. Nazeeruddin and V. Dyakonov, *J. Phys. Chem. C*, 2018, **122**, 22796. c) X. Cai, X. Li, G. Xie, Z. He, K. Gao, K. Liu, D. Chen, Y. Cao and S.-J. Su, *Chem. Sci.*, 2016, **7**, 4264; d) K. Goushi, K. Yoshida and K. Sato, C. Adachi, *Nat. Photon.*, 2012, **6**, 253; e) Q. Zhang, H. Kuwabara, W. J. Potscavage, S. Huang, Y. Hatae, T. Shibata and C. Adachi, *J. Am. Chem. Soc.*, 2014, **136**, 18070;

[5] N. Nijegorodov, V. Zvolinsky and P. V. C. Luhanga, *J. Photochem. Photobiol. A: Chem.* 2008, **196**, 219.

[6] D. Hu, L. Yao, B. Yang and Y. Ma, *Philos Trans A Math Phys Eng Sci*, 2015, **373**.

[7] H. Tanaka, K. Shizu, H. Miyazaki and C. Adachi, *Chem. Commun.*, 2012, **48**, 11392.

[8] Y. Jia, Y. Zhang, S. Fan, S. Wu, X. Zhao and S. Wang, X. Li, *Org. Electron*., 2019, **64**, 259.

[9] X. Qiu, S. Ying, C. Wang, M. Hanif, Y. Xu, Y Li, R. Zhao, D. Hu, D. Ma and Y. Ma, *J. Mater. Chem. C*. 2019, **7**, 592.

[10] W. Liu, S. Ying, R. Guo, X. Qiao, P. Leng, Q. Zhang, Y. Wang, D. Ma and L. Wang, *J. Mater. Chem. C.*, 2019, **7**, 1014.

[11] W.-C. Chen, Y. Yuan, Z.-L. Zhu, Z.-Q. Jiang, L.-S. Liao and C.-S. Lee, *Adv. Optical Mater*., 2018, **6**, 1700855.

[12] W. Zhang, Y.-X. Zhang, X.-Q. Zhang, X.-Y. Liu, J. Fan and L.-S. Liao, *Org. Electron*., 2018, **58**, 238.

[13] J. Zhao, B. Liu, Z. Wang, Q. Tong, X. Du, C. Zheng, H. Lin, S. Tao and X. Zhang, *ACS Appl. Mater. Interface*s., 2018, **10**, 9629.

[14] J. Shi, Q. Ding, L. Xu, X. Lv, Z. Liu, Q. Sun, Y. Pan, S. Xue and W. Yang, *J. Mater. Chem. C*., 2018, **6**, 11063.

[15] M. Bian, Z. Zhao, Y. Li, Q. Li, Z. Chen, D. Zhang, S. Wang, Z. Bian, Z. Liu, L. Duan and L. Xiao, *J. Mater. Chem. C*., 2018, **6**, 745.

[16] Y.-X. Zhang, Y. Yuan, Q. Wang, Y. Hu, A. Khan, Z.-Q. Jiang and L.-S. Liao, *Dyes Pigments*., 2018, **158**, 396.

[17] S. Peng, Y. Zhao, C. Fu, X. Pu, L. Zhou, Y. Huang and Z. Lu, *Chem. Eur. J*. 2018, **24**, 8056.

[18] J. Jayabharathi, P. Sujatha, V. Thanikachalam and P. Nethaji, *RSC Adv*. 2018, **8**, 20007.

[19] S. Wang, M. Qiao, Z. Ye, D. Dou, M. Chen, Y. Peng, Y. Shi, X. Yang, L. Cui, J. Li, C. Li, B. Wei and W.-Y. Wong, *iScience*., 2018, **9**, 532.

[20] N. Jürgensen, A. Kretzschmar, S. Höfle, J. Freudenberg, U. H. F. Bunz and G. Hernandez-Sosa, *Chem. Mater*., 2017, **29**, 9154.

[21] Z.-L. Zhu, S.-F. N, W.-C. Chen, Y. Yuan, Q.-X. Tong, F.-L. Wong, F. Lu and C.-S. Lee, *Dyes Pigments*. 2017, **146**, 219.

[22] W.-C. Chen, Y. Yuan, Y. Xiong, A. L. Rogach, Q.-X. Tong and C.-S. Lee, *ACS Appl. Mater. Interfaces*., 2017, **9**, 26268.

[23] X. Du, G. Li, J. Zhao, S. Tao, C. Zheng, H. Lin, Q. Tong and X. Zhang, *Adv. Optical Mater*., 2017, **5**, 1700498.

[24] B. Li, G. Tang, L. Zhou, D. Wu, J. Lan, L. Zhou, Z Lu and J. You, *Adv. Funct. Mater*., 2017, **27**, 1605245.

[25] B. Liu, Z.-W. Yu, D. He, Z.-L. Zhu, J. Zheng, Y.-D. Yu, W.-F. Xie, Q.-X. Tong and C.-S. Lee, *J. Mater. Chem. C.*, 2017, **5**, 5402.

[26] L.-S. Cui, H. Nomura, Y. Geng, J. U. Kim, H. Nakanotani and C. Adachi, *Angew. Chem. Int. Ed. Engl.*, 2017, **56**, 1571.

[27] A. Obolda, Q. Peng, C. He, T. Zhang, J. Ren, H. Ma, Z. Shuai and F. Li, *Adv. Mater.*, 2016, **28**, 4740.

[28] G. Li, J. Zhao, D. Zhang, Z. Shi, Z. Zhu, H. Song, J. Zhu, S. Tao, F. Lu and Q. Tong, *J. Mater. Chem. C.*, 2016, **4**, 8787.

[29] Y.-H. Chen, C.-C. Lin, M.-J. Huang, K. Hung, Y.-C. Wu, W-C. Lin, R.-W. Chen-Cheng, H.-W. Lin and C.-H. Cheng, *Chem. Sci.*, 2016, **7**, 4044.

[30] X. Tang, Q. Bai, Q. Peng, Y. Gao, J. Li, Y. Liu, L. Yao, P. Lu, B. Yang and Y. Ma, *Chem. Mater.*, 2015, **27**, 7050.

[31] J.-H. Jou, S. Kumar, P.-H. Fang, A. Venkateswararao, K. Thomas, J.-J. Shyue, Y.-C. Wang, T.-H. Li and H.-H. Yu, *J. Mater. Chem. C.*, 2015, **3**, 2182.

[32] C. He, H. Guo, Q. Peng, S. Dong and F. Li, *J. Mater. Chem. C.* 2015, **3**, 9942.

[33] S. Cha, N. Han, J. Song, S.-R. Park, Y. Jeon and M. Suh, *Dyes Pigments.*, 2015, **120**, 200.

[34] W.-C. Chen, Y. Yuan, G.-F. Wu, H.-X. Wei, J. Ye, M. Chen, F. Lu, Q.-X. Tong, F.-L. Wong and C.-S. Lee, *Org. Electron.*, 2015, **17**, 159.

[35] J.-Y. Hu, Y.-J. Pu, F. Satoh, S. Kawata, H. Katagiri, H. Sasabe and J. Kido, *Adv. Funct. Mater.*, 2014, **24**, 2064.

[36] S. Tang, W. Li, F. Shen, D. Liu, B. Yang and Y. Ma, *J. Mater. Chem.*, 2012, **22**, 4401.

[37] C.-J. Zheng, W.-M. Zhao, Z.-Q. Wang, D. Huang, J. Ye, X.-M. Ou, X.-H. Zhang, C.-S. Lee and S.-T. Lee, *J. Mater. Chem.*, 2010, **20**, 1560.

[38] L. Wang, Y. Jiang, J. Luo, Y. Zhou, J. Zhou, J. Wang, J. Pei and Y. Cao, *Adv. Mater.*, 2009, **21**, 4854.

[39] C.-J. Kuo, T.-Y. Li, C.-C. Lien, C.-H. Liu, F.-I. Wu and M.-J. Huang, *J. Mater. Chem.*, 2009, **19**, 1865.

[40] O. V. Dolomanov, L. J. Bourhis, R. J. Gildea, J. A. K. Howard and H. Puschmann, *J. Appl. Crystallogr.*, 2009, **42**, 339.

[41] L. J. Bourhis, O. V. Dolomanov, R. J. Gildea, J. A. K. Howard and H. Puschmann, *Acta Crystallogr. A.*, 2015, **71**, 59.

[42] D. Kratzert, J. J. Holstein and I. Krossing, *J. Appl. Crystallogr.*, 2015, **48**, 933.

[43] L. Palatinus, S. J. Prathapa and S. van Smaalen, *J. Appl. Crystallogr.*, 2012, **45**, 575.

[44] G. Sheldrick, *Acta Crystallogr. C.*, 2015, **71**, 3.

[45] Z. K. Chen, W. Huang, L. H. Wang, E. T. Kang, B. J. Chen, C. S. Lee and S. T. Lee, *Macromolecules*, 2000, **33**, 9015.

[46] M. J. Frisch, G. W. Trucks, H. B. Schlegel, G. E. Scuseria, M. A. Robb, J. R. Cheeseman, G. Scalmani, V. Barone, B. Mennucci, G. A. Petersson, H. Nakatsuji, M. Caricato, X. Li, H. P. Hratchian, A. F. Izmaylov, J. Bloino, G. Zheng, J. L. Sonnenberg, M. Hada, M. Ehara, K. Toyota, R. Fukuda, J. Hasegawa, M. Ishida, T. Nakajima, Y. Honda, O. Kitao, H. Nakai, T. Vreven, J. A. Montgomery, J. E. Peralta, F. Ogliaro, M. Bearpark, J. J. Heyd, E. Brothers, K. N. Kudin, V. N. Staroverov, R. Kobayashi, J. Normand, K. Raghavachari, A. Rendell, J. C. Burant, S. S. Iyengar, J. Tomasi, M. Cossi, N. Rega, J. M. Millam, M. Klene, J. E. Knox, J. B. Cross, V. Bakken, C. Adamo, J. Jaramillo, R. Gomperts, R. E. Stratmann, O. Yazyev, A. J. Austin, R. Cammi, C. Pomelli, J. W. Ochterski, R. L. Martin, K. Morokuma, V. G. Zakrzewski, G. A. Voth, P. Salvador, J. J. Dannenberg, S. Dapprich, A. D. Daniels, Ö. Farkas, J. B. Foresman, J. V. Ortiz, J. Cioslowski Fox, D. J. Gaussian 09; Gaussian, Inc.: Wallingford CT, 2009.

[47] a) A. D. Becke, *J. Chem. Phys.*, 1993, **98**, 5648; b) C. Lee, W. Yang and R. G. Parr, *Phys. Rev. B*, 1988, **37**, 785.

[48] a) R. Bauernschmitt, M. Häser, O. Treutler and R. Ahlrichs, *Chem. Phys. Lett.*, 1997, **264**, 573; b) R. E. Stratmann, G. E. Scuseria and M. J. Frisch, *J. Chem. Phys.*, 1998, **109**, 8218.

[49] E. Cancès, B. Mennucci and J. Tomasi, *J. Chem. Phys.*, 1997, **107**, 3032.

[50] P. L. Santos, J. S. Ward, P. Data, A. S. Batsanov, M. R. Bryce, F. B. Dias and A. P. Monkman, *J. Mater. Chem. C*, 2016, **4**, 3815.

[51] T. Wang, N. Zhang, K. Zhang, J. Dai, W. Bai and R. Bai, *Chem. Commun.*, 2016, **52**, 9679.

[52] H. Gilman and J. Diehl, *J. Org. Chem.*, 1959, **24**, 1914.

[53] J. Yang, Q. Guo, J. Wang, Z. Ren, J. Chen, Q. Peng, D. Ma and Z. Li, *Adv. Opt. Mater.*, 2018, **6**, 1800342.

IV. Copies of NMR spectra of compounds

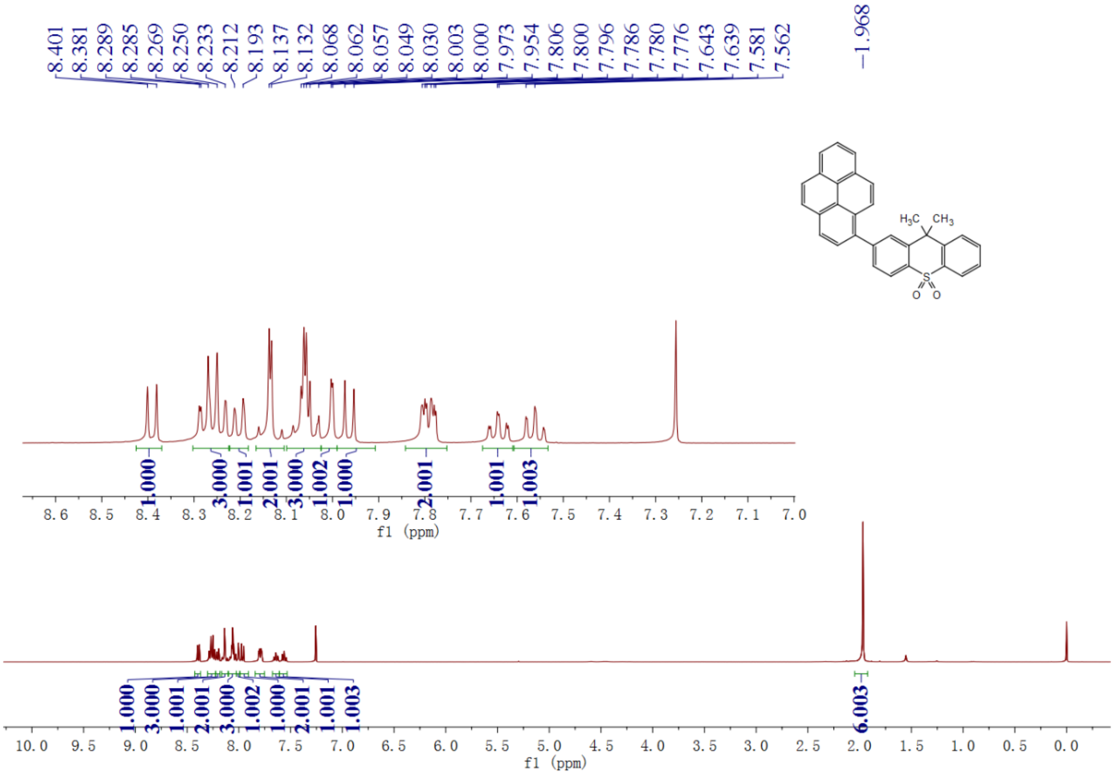

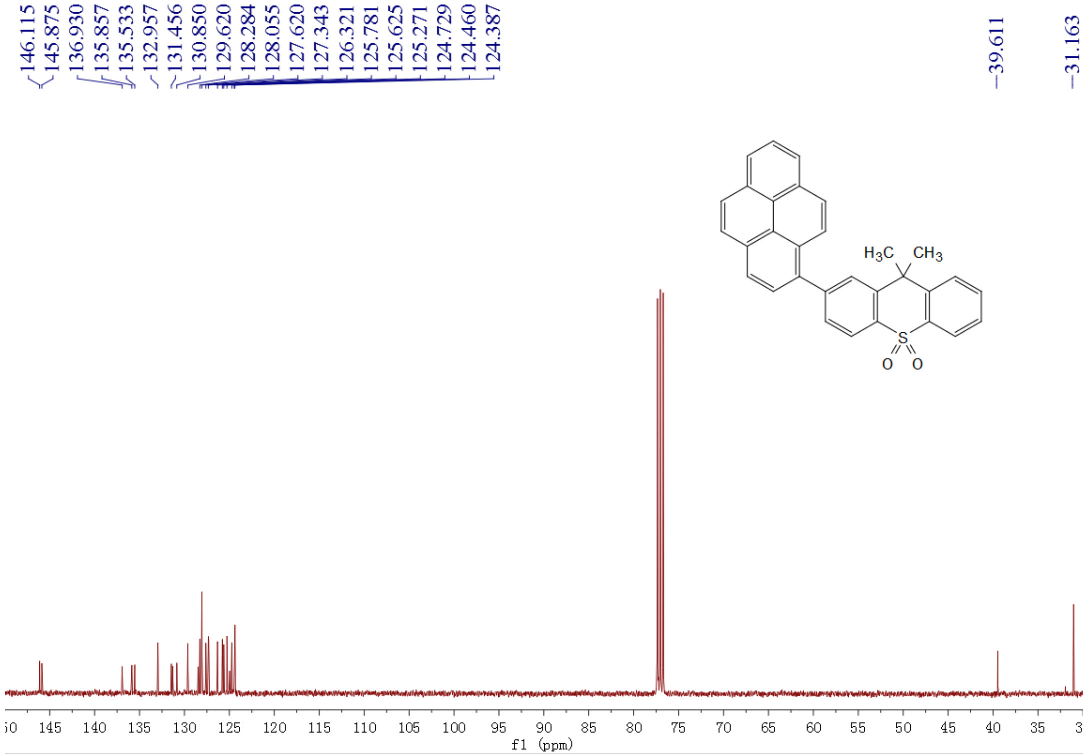

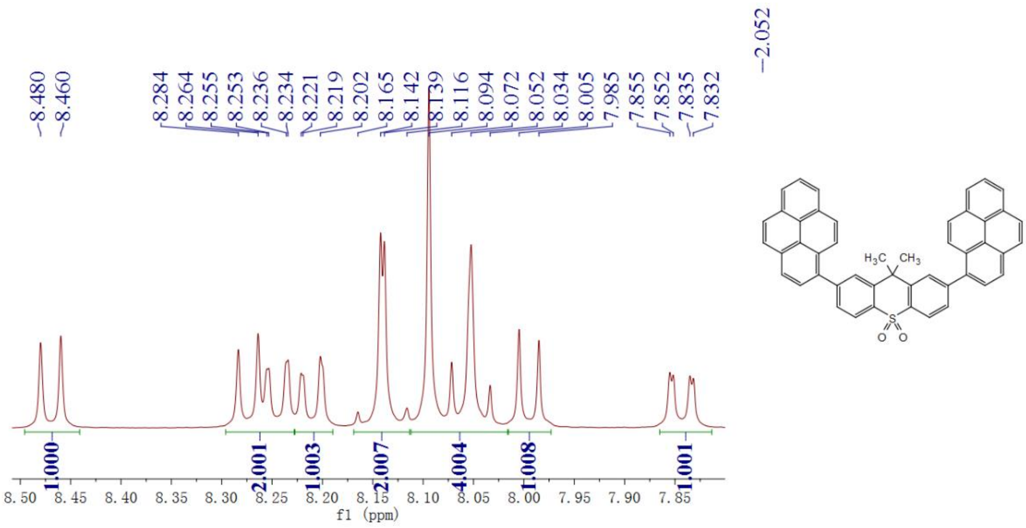
8.480
8.460
8.284
8.264
8.255
8.253
8.236
8.234
8.221
8.219
8.202
8.165
8.142
8.139
8.116
8.094
8.072
8.052
8.034
8.005
7.985
7.855
7.852
7.835
7.832
2.052
1.000
2.001
1.003
2.007
4.004
1.008
1.001
8.50 8.45 8.40 8.35 8.30 8.25 8.20 8.15 8.10 8.05 8.00 7.95 7.90 7.85
f1 (ppm)
H3C CH3
S
O O

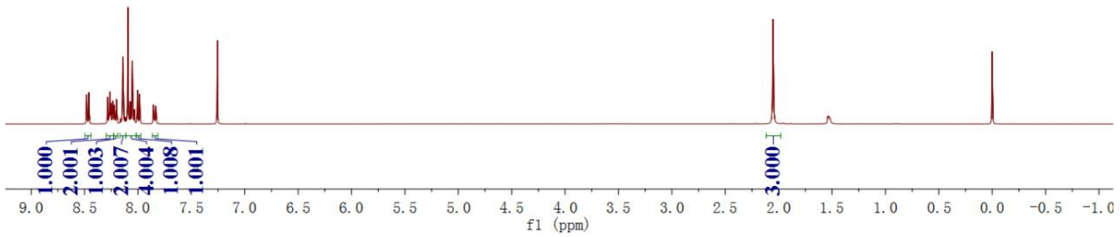
1.000
2.001
1.003
2.007
4.004
1.008
1.001
3.000
9.0 8.5 8.0 7.5 7.0 6.5 6.0 5.5 5.0 4.5 4.0 3.5 3.0 2.5 2.0 1.5 1.0 0.5 0.0 -0.5 -1.0
f1 (ppm)

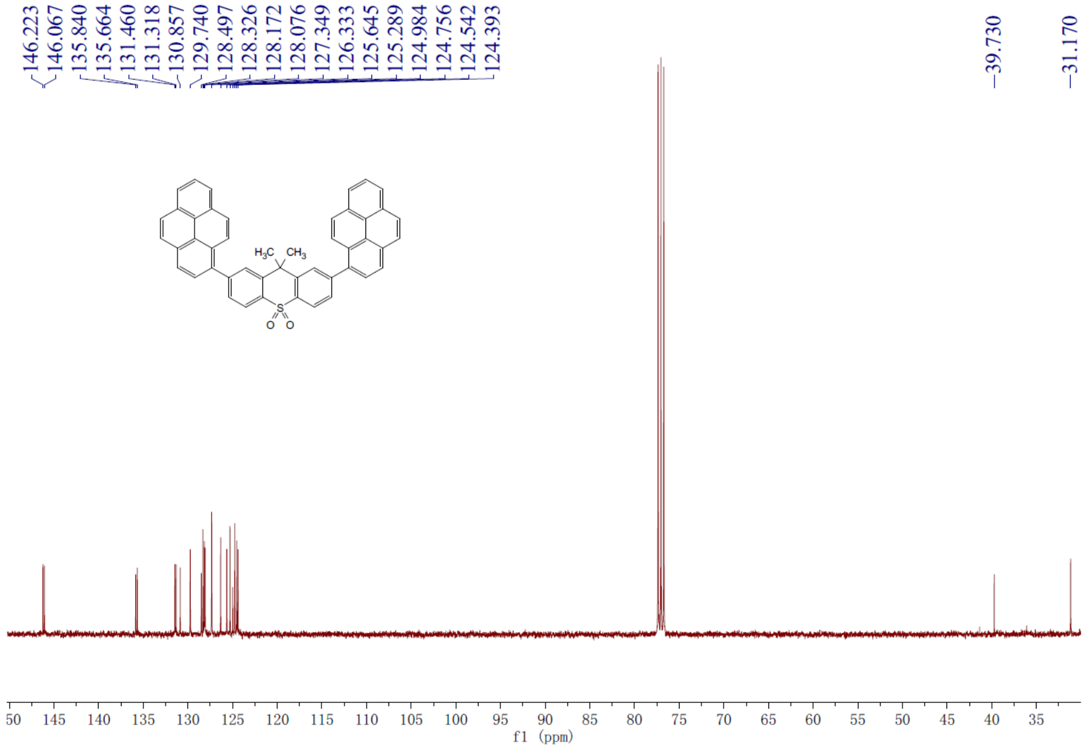
146.223
146.067
135.840
135.664
131.460
131.318
130.857
129.740
128.497
128.326
128.172
128.076
127.349
126.333
125.645
125.289
124.984
124.756
124.542
124.393
39.730
31.170
H3C CH3
S
O O
50 145 140 135 130 125 120 115 110 105 100 95 90 85 80 75 70 65 60 55 50 45 40 35
f1 (ppm)

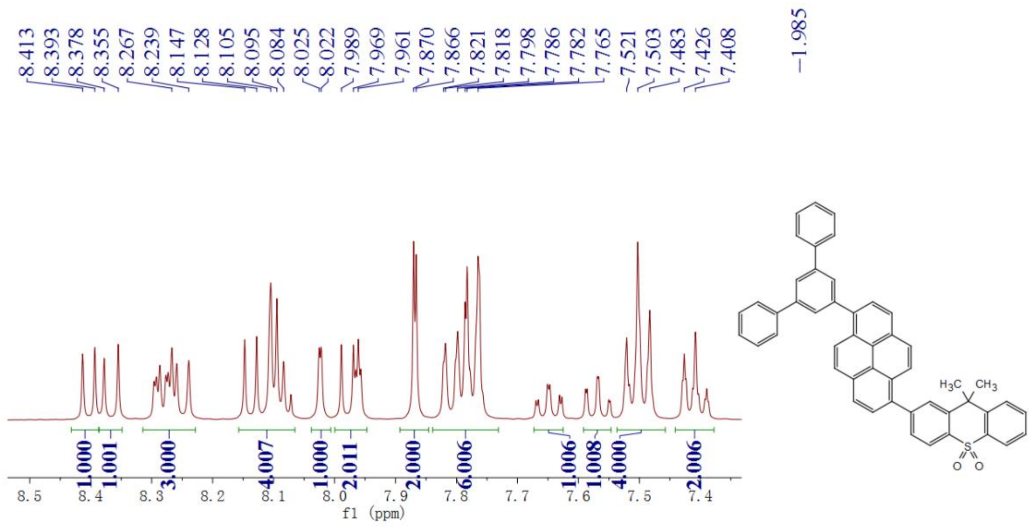
8.413
8.393
8.378
8.355
8.267
8.239
8.147
8.128
8.105
8.095
8.084
8.025
8.022
7.989
7.969
7.961
7.870
7.866
7.821
7.818
7.798
7.786
7.782
7.765
7.521
7.503
7.483
7.426
7.408
1.985
1.000
1.001
3.000
4.007
1.000
2.011
2.000
6.006
1.006
1.008
4.000
2.006
8.5
8.4
8.3
8.2
8.1
8.0
7.9
7.8
7.7
7.6
7.5
7.4
f1 (ppm)
H_3C
CH_3
S
O
O

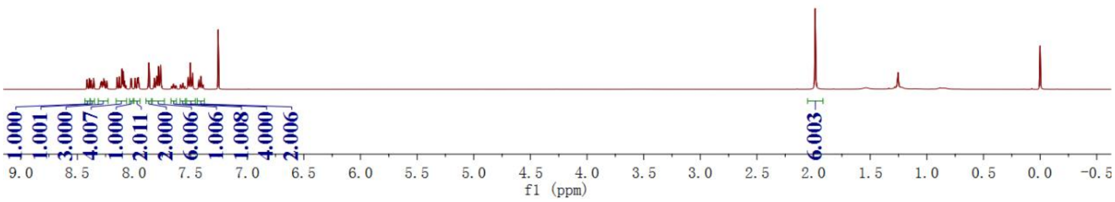
1.000
1.001
3.000
4.007
1.000
2.011
2.000
6.006
1.006
1.008
4.000
2.006
6.003
9.0
8.5
8.0
7.5
7.0
6.5
6.0
5.5
5.0
4.5
4.0
3.5
3.0
2.5
2.0
1.5
1.0
0.5
0.0
-0.5
f1 (ppm)

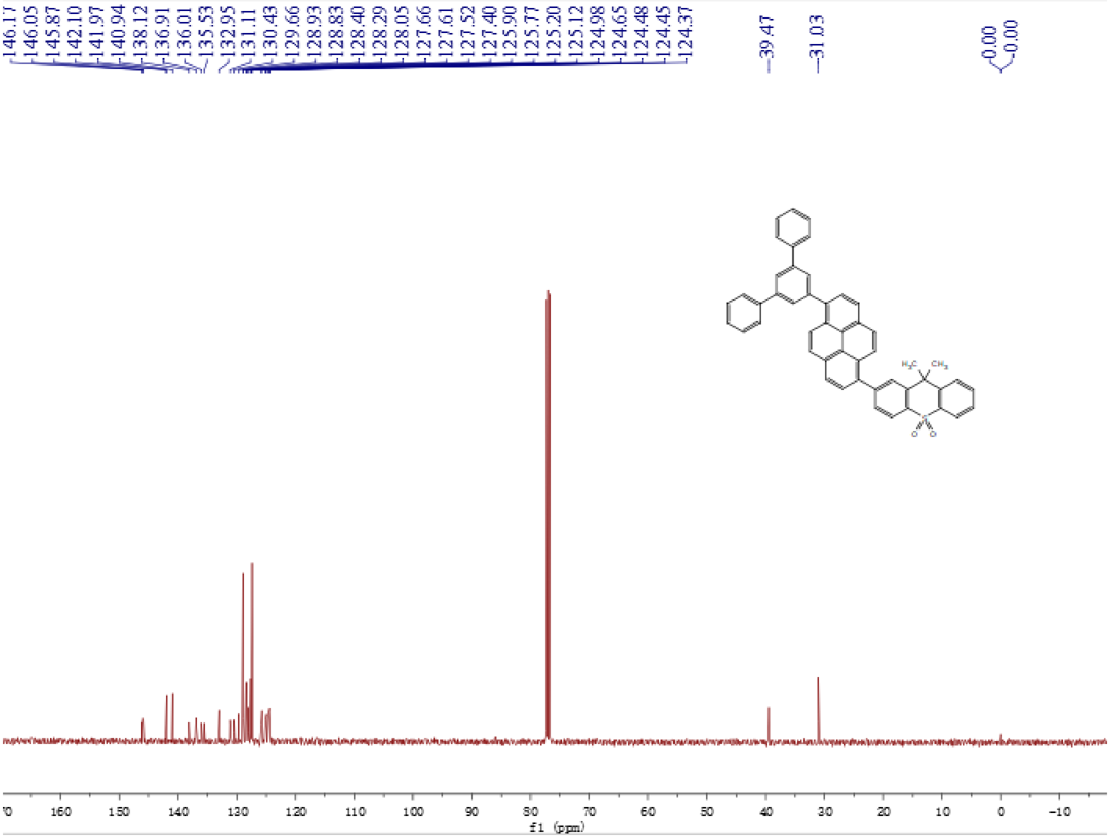
146.17
146.05
145.87
142.10
141.97
140.94
138.12
136.91
136.01
135.53
132.95
131.11
130.43
129.66
128.93
128.83
128.40
128.29
128.05
127.66
127.61
127.52
127.40
125.90
125.77
125.20
125.12
124.98
124.65
124.48
124.45
124.37
39.47
31.03
0.00
0.00
H_3C
CH_3
S
O
O
160
150
140
130
120
110
100
90
80
70
60
50
40
30
20
10
0
-10
f1 (ppm)

V. Copies of HR-MS spectra characterization results of compounds.